Chapter 15 Pitfalls in Ion Beam Analysis

C. Jeynes

University of Surrey Ion Beam Centre, Guildford, England

N. P. Barradas

Instituto Tecnológico e Nuclear, Sacavém, Portugal

Centro de Física Nuclear da Universidade de Lisboa, Lisboa, Portugal

Contributors: M. Döbeli, J. A. Davies, W. N. Lennard, and I. V. Mitchell

CONTENTS

15.1 INTRODUCTION

Ion beam analysis (IBA) is a quantitative analytical technique, and in this chapter, we intend to show how to avoid many pitfalls when determining elemental depth profiles accurately with light-ion Rutherford backscattering spectrometry (RBS) using megaelectronvolt ion beams. IBA can, of course, use various other beams and use these for a variety of other purposes, including profiling of crystalline defects. The present discussion is usually, but not always, easily generalized to these other cases. We will therefore also cover pitfalls in a number of other important examples.

We will, in general, be guided by Chapter 12 of the previous edition of this handbook (Tesmer and Nastasi, 1995). However, that chapter contains many subtle discussions that we will avoid or simplify, referring the advanced IBA user back to it. Today, most laboratories that are starting to use IBA have the new generation of accelerators, eliminating many of the problems associated with the older accelerators that the previous chapter addressed.

A new generation of software is available that renders obsolete many of the numerical examples of the previous handbook. We will assume that users interested in accurate work will have access to one of the codes described and evaluated in the 2006 International Atomic Energy Agency (IAEA) sponsored IBA software intercomparison exercise (Barradas *et al.*, 2007, 2008), where it is shown that IBA spectra can be treated numerically with a confidence of about 0.2% and that, currently, the best absolute experimental accuracy available is 0.6%. Data analysis software for IBA is discussed in Chapter 14. We therefore intend to describe sources of error (pitfalls) greater than about 0.25%; we believe that users should be aiming at accuracies of 1% or better.

The nuclear physics background of the old generation of IBA practitioners has become inaccessible to many of today's users; IBA is of great value in materials characterization and is used increasingly by materials scientists who have not had a nuclear physics training. This chapter is intended to be of particular value to this type of user.

Accurate elemental depth profiling by IBA is of great value in many modern thin-film technologies: the most obvious comparable technique is secondary ion mass spectrometry (SIMS), which is often used for these types of problems. SIMS is a powerful and sensitive technique, but it is usually only semiquantitative, and it is generally unreliable at interfaces (unless the system is well known). IBA, on the other hand, is particularly good at interfaces and has an accuracy that is easily traceable to international standards, making it suitable for standards work. We show in this chapter how to best capitalize on these strengths.

For parts of this chapter, we take a measurement of the implanted fluence of As into Si (Jeynes *et al.*, 2006) as a worked example of various pitfalls in doing accurate IBA. The collected spectra are shown in Fig. 15.1. Two important equations are relevant to this discussion: Equation 15.1 simply describes the number N_A (in atoms/cm^2) of As atoms, which is given by the measured area A_A of the signal of element A (in this particular example, A is As) (in counts)

$$A_A = QN_A\sigma'_A(E,\theta)\Omega\,, \tag{15.1}$$

where Q is the number of incident particles (the "collected charge") and Ω is the detector solid angle (in steradians, sr). σ'_A is the differential cross section (in cm^2/sr) of element A and is a function both of the scattering angle θ and of the beam energy E as it decreases from its initial energy, E_0, as it penetrates into the sample.

In Fig. 15.1, there are two signals of analytical interest. The first is obviously the As signal. However, in Eq. (15.1), we also need to know the product of the charge and the solid angle, $Q\Omega$. This is determined from the Si signal and the known energy loss of the He beam in a silicon matrix. For backscattering with the detector at an angle of θ to the beam and normal beam incidence, the surface yield, Y_0 (in counts/channel), for element A in matrix AB is given by the equation

$$Y_{0,A} = Qf_A \sigma'_A \Omega \Delta / [\varepsilon_0]_A^{AB}, \tag{15.2}$$

where f_A is the fraction of the matrix that is element A, Δ is the electronic gain (in eV/channel of the analog–digital converter), and $[\varepsilon_0]_A^{AB}$ (in eV cm^2) is the energy-loss factor for the signal of A from the surface of matrix AB given the beam energy and the scattering angle (see Chapter 4).

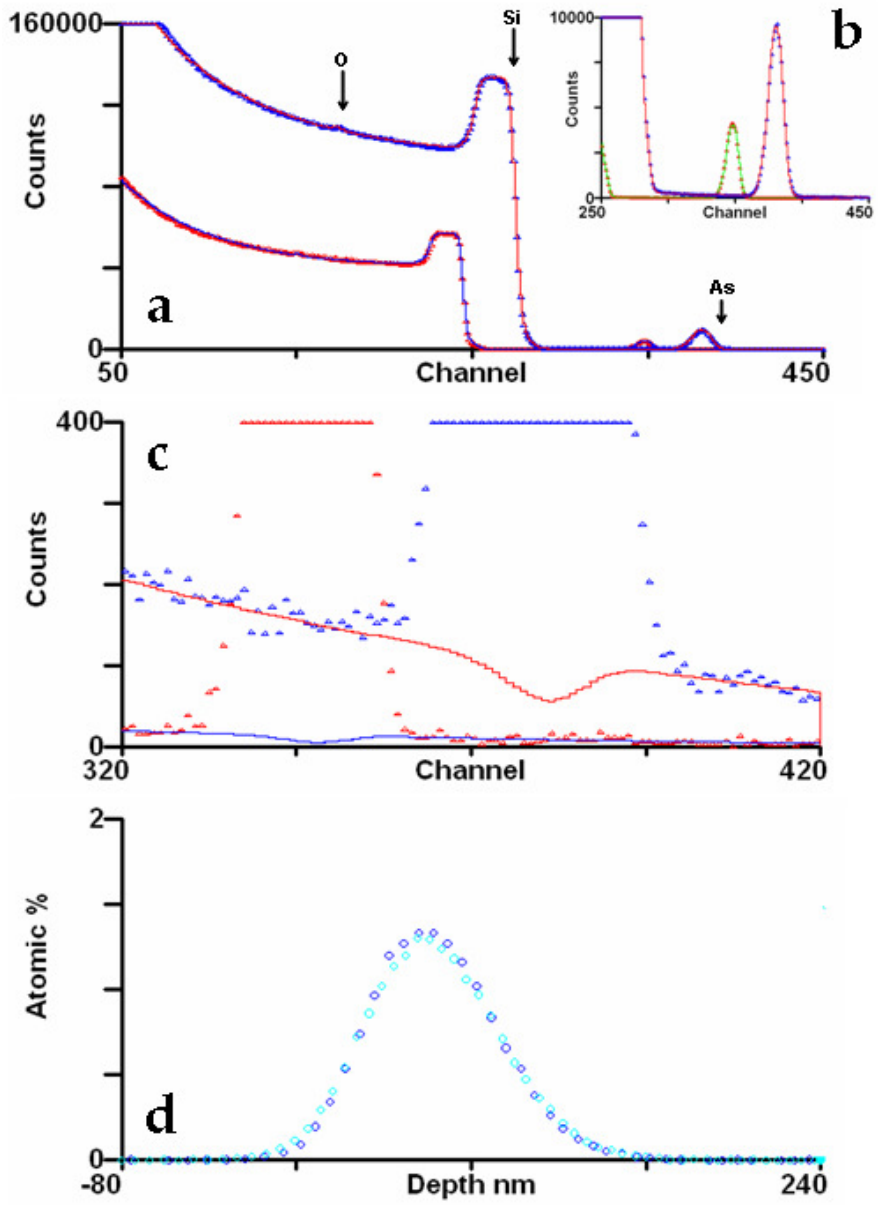

FIG. 15.1. Accurate analysis of As implanted fluence in Si. (a) Nominal implant 5×10^{15} As/cm^2 at 100 keV. 1.5 MeV He RBS spectra from two detectors collected simultaneously, and 0.5 mC collected charge, with fits. The beam is incident normally on the sample such that it channels in the substrate, and the near-surface region of silicon amorphized by the ion beam is clearly seen. A small O peak from the surface oxide is also clearly distinguishable. The As, Si, and O edges are marked for the detector with the larger solid angle. (b) Detail of the As signal. (c) Expanded detail of the As signal, with the nonlinear pileup correction function shown. (d) Pileup-corrected As signal from each detector plotted on a concentration versus depth scale (using a Si density of 5×10^{22}/cm^3). (Reproduced from Jeynes *et al.*, 2006.)

Equations (15.1) and (15.2) have been simplified without any loss of generality. They should both really be integrals over the depth of the signal, noticing that σ' varies as $1/E^2$, and that $[\varepsilon]$ is also a function of depth. The standard IBA codes have been validated to do these integrations correctly (Barradas *et al*., 2007, 2008).

For the example of Fig. 15.1, determining the number of As atoms present [using Eq. (15.1)] depends on an indirect measurement of the product of the charge and the solid angle, $Q\Omega$, from the height, Y, of the silicon substrate signal [using Eq. (15.2)], where the number of Si scattering centers is implicit in the $\Delta/[\varepsilon]$ ratio. In the rest of this chapter, we elaborate on various of the issues raised by these equations (as well as some others).

15.2 LOST BEAM AND EVENTS

15.2.1 Charge measurement

The collected charge Q in Eqs. (15.1) and (15.2) is a very important quantity that it is not very easy to measure. In the implantation of Fig. 15.1, the As implanted fluence was determined during the implantation by collecting charge in Faraday cups of the design shown in Fig. 15.2. This is a demanding application because large heavy-ion beam currents are used in implanters and the beam being measured usually falls only partially on the primary aperture. Jeynes *et al*. (2006) shows that this design is capable of charge measurement in this application with an accuracy of around 1%.

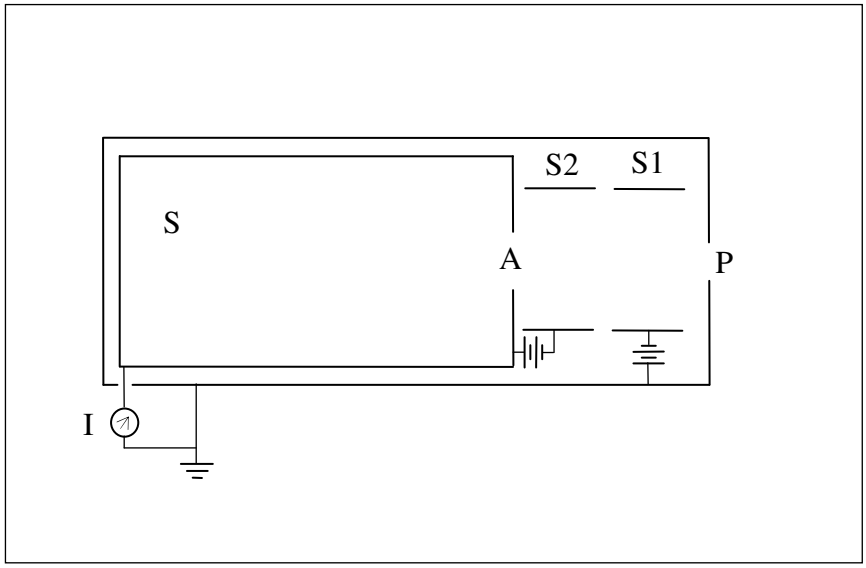

FIG. 15.2. Faraday cup design. The sensor S is an equipotential volume in a grounded case. Secondary electrons from the primary aperture P are suppressed by electrode S1, and any secondary electrons escaping through the secondary aperture A are suppressed by electrode S2. Suppression voltages are typically 300 V.

At issue is not the simple measurement of charge in a current integrator, which can (and should!) be calibrated against standard current sources with picoCoulomb accuracy. There are two points to note from Fig. 15.2. First, the incident beam will generate a large number of secondary electrons at the primary (beam-defining) aperture (P), many of which will have a significant momentum toward the target. The secondary electron current is usually comparable to the incident beam current and often exceeds it, in the case of heavy-ion beams, by orders of magnitude. It is important to carefully suppress such electrons.

Second, the beam striking the target will liberate many secondary electrons and photons (X-rays). Most of the secondary electrons will be low in energy (<10 eV), but a significant number will have high energies that could be on the order of kiloelectronvolts. Some electrons will therefore escape the Faraday cup (S) through the secondary aperture (A; this aperture is not struck by the primary beam) and must be suppressed. There is also the possibility that secondary positive ions (or low-energy multiply scattered primary ions) could also escape the Faraday cup; they will be attracted by the suppression electrode and will give rise to tertiary currents (which will be amplified by secondary electrons liberated and repelled from the suppression electrode by the ion impacts). Tertiary currents are not seen by the current integrator (I) in this design. These secondary particle effects can be very large for some insulating samples and at low (kiloelectronvolt) beam energies.

For IBA applications, such a well-designed Faraday cup is usually impractical, as the target might be large or part of a more or less complicated manipulator and, in any case, access is needed to the detector, which could be of various types (particle, photons including X-rays, time-of-flight, etc.) or in various geometries. However, when direct charge measurements are made, the geometry of the actual apparatus should be critically compared with the "ideal" Faraday cup described. It should be remembered that photon impact can also liberate secondary electrons, and for samples that generate many photons, this effect can be large (Venkatesan *et al.*, 1984).

Electron suppression can work just as well with magnetic fields as with electrostatic fields, and small, strong permanent magnets are now readily available. However, the use of electrostatic and magnetic fields together is to be avoided because, when both fields are present, electron paths can be very complicated and any possible escape paths will probably be found. With electrostatic fields, the suppressor action should be checked periodically, as insulating deposits can build up on the surfaces over time, attracting fixed charges that can entirely compensate the applied field.

A variety of methods have been used to determine collected charge apart from direct measurement from the target. Transmission Faraday cups were described by Sitter *et al.* (1982) and by Pászti *et al.* (1990). In both of these instruments, a rotating or reciprocating vane cuts the beam periodically, and the charge deposited on the vane is measured with a precision of about 1%. The pitfall to avoid in this sort of measurement is forgetting that the secondary electron yield is enormous when the beam strikes the edge of the vane and that suppression of these electrons is as important on the downside as on the upside of the vane. A passive instrument where a fixed mesh is used instead of a chopper was described by El Bouanani *et al.* (2006).

Rotating vane instruments were reported by Piel *et al.* (1994) and by Giuntini and Mando (1994) that collected backscattered particles from the vane, instead of charge. For these instruments, the vane is coated with gold, and the particles scattered from gold are discriminated in a single-channel analyzer (SCA). This is quite a troublesome arrangement because the signal changes for different beams and one really needs to see the spectrum to set up the SCA correctly. Users have also found that a gate is needed to exclude edge signals from the detector. It is possible, but not easy, to obtain excellent precision (1%) with such a design.

Transmission detectors take a fraction of the beam, of course, and this fraction must be measured directly with a downstream Faraday cup (which can be of ideal design). The great virtue of transmission detectors is that they are completely independent of the target, which can then be manipulated, be heated or cooled, or be made of any material without affecting the charge measurement in any way.

15.2.2 Beamline charge exchange

In modern systems with good vacuums, beamline charge exchange is an unusual problem. Users should be aware, however, that there is a possibility of significant beam charge exchange where the vacuum is poor. This problem was reviewed in considerable detail by Allison (1958). when it does occur, there is a probability both of lower and higher charge states.

Accelerators used for implantations often scan the ion beam to implant the sample uniformly, and in such beam lines, a "neutral trap" is always incorporated, where a neutral trap is a voltage applied to transmit the beam past a kink in the beam line. The neutral beam is not deflected and is intercepted by an aperture. For IBA, the beam lines do not always have neutral traps, and the beams are not usually scanned, so that neutral beams will give an unchanged IBA signal but will not be detected by the current integrator. Because the beam lines are usually long, the neutral fraction of the beam can be significant if the vacuum is poor.

Conversely, a He^+ beam can suffer further charge-stripping collisions, giving a significant He^{2+} component. As an example, if the beamline pressure is 1 mPa (10^{-5} mbar) and the beamline is 4 m long, then the neutralization probability for a 450 keV $^4He^+$ particle is about 1%, but the probability of electron stripping to form He^{2+} is higher at about 2%. For a 450 keV He^{2+} beam in this beamline, the probability of He^+ is 5%, but the probability of the neutral is only 0.5%. For three times the energy, one might expect the neutralization cross sections to fall by a factor 3 or so. The cross section for He^+ to change to He^{2+} falls from 66 megabarns (Mb) to 37 Mb as the He^+ energy increases from 450 keV to 1700 keV, but the cross section of the reverse charge exchange, of He^{2+} changing to He^+, falls from 170 Mb (for 450 keV He^{2+}) to 5 Mb (for 1700 keV He^{2+}).

15.2.3 Particle identification

A precise knowledge of the parameters of the incident particle is essential for all ion beam experiments. We assume here that the accelerator has only an analyzing magnet [with relatively poor mass resolution compared to that of accelerator mass spectrometry (AMS)] to perform momentum selection of the beam. Many accelerators suffer from periodic problems due to unwanted contaminant beams that arrive at the target together with the desired species. Such problems are caused by

- atomic or molecular particles whose kinematic properties mimic the acceleration and deflection kinematics of the desired particle,
- unwanted particles that reach the target because of a low-probability charge exchange sequence occurring upstream of the target, or
- particles that have completely incorrect kinematics but arrive at the target because of (wall) scattering.

One of the simplest ways to test for a mixture of "equal-mass" beams in single-ended machines is to detect elastically scattered projectiles from a thin self-supporting Au target. An energy spectrum analysis with a standard surface-barrier detector system will readily distinguish the fragments of molecular impurities, such as mixtures of H_3^+, HD^+, and $^3He^+$ or mixtures of $^4He^+$ and D_2^+, which can arise through ion-source memory effects.

The consequences of scattering the three ion species H_3^+, HD^+, and $^3He^+$ from a thin Au scattering foil, when the incident species have equal energy (1 MeV), are listed in Table 15.1. We assume that the detector is located at 90° (laboratory angle). The three beams would give rise to three distinct peaks:

- for H_3^+, a single peak at 0.33 MeV energy;
- for HD^+, two peaks corresponding to 0.33 MeV protons and 0.67 MeV deuterons; and
- for $^3He^+$, a single peak at 1 MeV energy.

The relative intensities are distinctive. The entries in Table 15.1 are based on a simple $(Z_1Z_2/E)^2$ dependence of the elastic (Rutherford) cross section for the dissociated fragments, with the kinematic factors approximated as unity.

Table 15.1: Relative particle yields and energies for several mass 3 ions incident on Au at 1 MeV.			
	Relative yield(s) of scattered particle(s)		
Beam	**H 0.33 MeV**	**D 0.67 MeV**	**^{3}He 1.0 MeV**
H_3^+	27		
HD^+	9	2.25	
$^{3}He^+$			4

Another example of the use of this Au foil scattering technique is the identification of ^{16}O ions in the presence of ^{4}He ions—a curiosity observed by Hemment *et al.* (1975) when poor beamline vacuum developed, thereby allowing a $^{16}O^+$ impurity beam co-accelerated to 2 MeV with the $^{4}He^+$ beam to undergo charge exchange to form $^{16}O^{2+}$ in the drift section between the accelerator and the analyzing magnet. This process allowed two beams of "identical" rigidity, ME/q^2 = 8 MeV amu, to be passed by the magnet.

The molecular interferences are not problematic for tandem-type accelerators, where there is an injection magnet at the source, an analyzing magnet following acceleration, and a (collisional) stripping event at the high-voltage terminal.

Wall scattering can be minimized using a series of apertures; however, care must be exercised so as not to restrict beamline pumping speed excessively.

15.2.4 Dead time and pulse pileup

We restrict our comments to "singles" experiments (as opposed to coincidence experiments) and solid-state detectors, which are most common for ion beam analysis applications, although much of this section is common to all types of analysis.

Dead time is generated in the counting system by the time taken to process each pulse. This is typically dominated by the analog-to-digital conversion (ADC) time (on the order of 10 μs) for particle detectors and by the preamplifier pulse processing time for Si(Li) X-ray detectors (typically greater than 10 μs). In all systems, the ADC should be capable of reporting to the user the actual dead time for each counting channel. This dead time must include any time spent in handshaking between the various electronic components. Where the ADC is a multichannel analyzer (MCA) or where the host computer is multitasking, there could be significant extra system dead time that affects all channels. In any case, where multiple detectors are used simultaneously, it is more important to accurately determine the relative live charge between the detectors than it is to determine the charge that fell on the sample (the true charge) during the collection time. For accurate work, it is essential to understand the operation of your spectroscopy system in detail.

Pulse pileup occurs when separate pulses come too close together in time and are not recognized as separate by the spectroscopy system. There are two cases for pulse pileup depending on whether a pileup rejection (PUR) circuit is present or not. Where PUR is used, pileup events will still occur because every spectroscopy system has a pulse detection time resolution and there is a nonzero probability for pulses to occur at any time separation, even simultaneously. Surface barrier detector preamplifiers, for example, can have a rise time of about 30 ns, and a typical resolution time for an amplifier PUR circuit is 500 ns. However, where PUR is used, any pileup events that are not rejected are considered nearly simultaneous, that is, the amplitude of the resulting sum pulse is

nearly the sum of the amplitudes of the pileup pulses. Where PUR is not used, the sum pulse can be of (nearly) any amplitude.

It is possible to eliminate pileup almost completely by determining both the momentum and the energy of the detected particles using a ΔE–E detector telescope (Gurbich, 1996) or using a time-of-flight detector with a pulsed incident ion beam (Gurbich and Kornilov, 1991). However, these approaches are significantly more complex, and the ΔE–E method requires very thin ΔE detectors for lower-energy He beams. instead, we concentrate here on correcting spectra collected with the simplest detectors.

Figure 15.3 shows a spectrum with significant pileup (and with PUR). The Au signal appears at channel 150, and the electronic pulser signal appears at channel 480. All of the counts above the Au signal are pileup counts (except for the pulser), and the shape of the pileup signal is recognizably an autoconvolution of the spectrum. The two-pulse pileup is accurately calculated (with or without PUR) with the algorithm of Wielopolski and Gardner (W&G) (Wielopolski and Gardner, 1976, 1977; Gardner and Wielopolski, 1977). This is a slow calculation, involving $n_{channel}^3$ operations, where $n_{channel}$ is the number of channels. The autoconvolution method (van Lieshout *et al.*, 1966), improved by Amsel *et al.* (1992), is faster given that it involves only $n_{channel}^2$ operations, but it is not as accurate. Where the pileup correction is significant, the best calculation should be done: refer to the manual for the IBA code being used to determine what this is. Some codes will also make an approximate calculation of three-pulse pileup (e.g., Barradas and Jeynes, 2008). We note that the best pileup calculations for most current particle-induced X-ray emission (PIXE) codes do not use the best algorithms (Barradas and Reis, 2006). We note also that the W&G algorithm assumes parabola-shaped pulses but can be extended to other shapes as well, and it requires knowledge of the time for a pulse to reach the maximum, which depends on the amplifier used (normally given in the amplifier documentation).

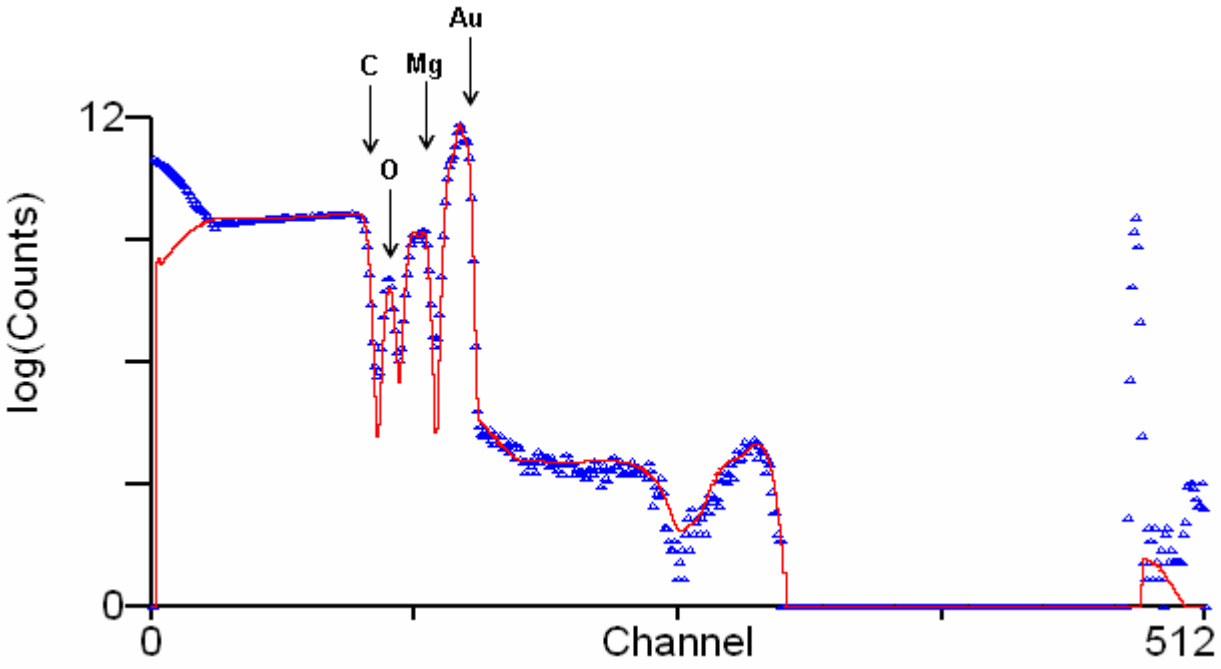

FIG. 15.3. Pileup with pileup rejection. Data obtained from 707 keV $^1H^+$ RBS of a Au/Mg multilayer on C, with a count rate of 4.3 kHz, an amplifier shaping time of 500 ns, and a PUR time resolution of 550 ns. A distinct O contamination peak can also be seen. Fit including pileup calculated with Wielopolski and Gardner's algorithm is as a solid line.

The W&G algorithm was applied in Fig. 15.1(c) to determine the pileup correction function of the As signal. This figure illustrates a dangerous pitfall: One might think that this pileup background is nicely linear from the pileup behaviors above and below the signal. However, it is very clear from

the calculated pileup signal shown that the pileup is actually strongly nonlinear. Of course, the pileup at any channel is the sum of the pileup events that are detected in that channel and events that should be in that channel but that are actually piled up and end up in higher channels. For strong signals, the pileup background can be negative because the latter events outweigh the former. For example, the Au signal of Fig. 15.3 is underestimated by 1.5% even for the relatively low count rate of 4 kHz.

Notice in Fig. 15.3 that, below about channel 30 there is a large "noise" signal. Usually, this is discriminated by the lower-level discriminator (LLD) of the amplifier to reduce the count rate into the ADC, but pileup will occur anyway, regardless of whether the (real) counts appear in the spectrum. In this case, the LLD was on, but an assumed (*ad hoc*) signal was arbitrarily included in the spectrum shown, such that the pileup above the Au edge and above the pulser signal were correctly reproduced. The extra (unfitted) counts above about channel 505 are an artifact of the ADC, which integrates all of the high-energy counts instead of truncating them. The pitfall to avoid is relying on even a good pileup calculation such as W&G too near a leading edge where the LLD will distort the calculated pileup signal.

When doing accurate work that depends on a good pileup calculation, it is important to use a constant beam current. The algorithms used by IBA codes take the live time as the input from which the average count rate is calculated. If the count rate fluctuates, the pileup cannot be calculated accurately. The W&G calculation has no free parameters, although the collection time, the shaping time, and the PUR time resolution can be treated as fitting parameters. Analysts should note that large, rapid fluctuations in the incident beam intensity described by Sjöland *et al.* (1999) invalidate the simple W&G calculation, and every effort should be made to avoid fluctuating beams. Thankfully, modern accelerators generate very constant beam currents. Sjöland *et al.* (1999) also describe the more difficult case of scanning microbeam PIXE, where, even if the beam current is constant, the count rate generally is not.

Dead time and pileup arise in all of the electronic components (preamplifier, amplifier, ADC, etc.) because of the pulse rate. Solid-state detectors should be operated at pulse rates such that the pulses are separated by an average time interval that is much greater than the dead time inherent in the rest of the electronic circuitry. A 10-μs dead time per pulse implies a maximum counting rate of 100 kHz, but of course, the pulses come randomly in time, and dead time will increase rapidly (and nonlinearly) for count rates higher than about 10 kHz.

It is a good practice to always use a test pulse (see the pulser signal at channel 480 of Fig. 15.3) at the appropriate preamplifier input, that is, to introduce a signal that is periodic with known frequency (typically about 60 Hz). Thus, the total number of "missing" pulses due to count-rate losses during the acquisition time can be calculated from the measured area under the pulser peak. If the pulser is gated for dead time, then it will reflect pileup losses. When using a Faraday cup that rotates into the beam periodically, there are no pulser losses when the beam is hitting the cup. Here, the precise duty cycle of the cup must be measured, and its effect must be factored into the correction. Another way to measure counting losses using a pulser is to trigger the pulser with an output (usually scaled) from the current integrator. This way, if the beam goes off, so do the pulses, and because one usually counts for a preset charge, the number of pulses is also known. The pulser is in any case valuable for monitoring the stability of the electronics during the data collection run and also for monitoring the noise performance of the system.

In general, counting-rate losses will be nonnegligible for total pulse counting rates exceeding 1 kHz, which applies to almost all RBS measurements. Raising the LLD of the amplifier and/or ADC can decrease the dead-time problem, provided that the low-energy region of the spectrum is extraneous to the experiment (but doing so will also distort the pileup calculation as described in the preceding paragraphs). See Knoll's excellent text (1989) for more detail.

To conclude this section, we urge the reader to avoid the pitfall of counting too slowly in an attempt to avoid pileup and dead-time effects. It is a misuse of spectroscopic electronics of excellent

linearity—and of highly expensive accelerator facilities—not to count as fast as is feasible. We emphasize that the W&G pileup calculation is exact for two-pulse pileup (for parabolic pulses) and good-quality electronics will also give very precise dead-time values, so there is no need to reduce the count rate to avoid these effects, except, of course, where the signal-to-noise ratio is critical, such as when looking for trace heavy elements in a light matrix where the background is all from pileup. In any case, there are diminishing returns for decreasing the counting rate, as pileup is linear with counting rate and so is dead time for low count rates.

Count fast and do the corrections correctly!

15.2.5 Electronic noise and ground loops

State-of-the-art ion-implanted silicon detectors reach an energy resolution of 10 keV [full width at half-maximum (fwhm)] for helium ions and 5 keV for protons. The contribution of electronic noise from a standard preamplifier is about 3 keV. For high-resolution measurements, it is therefore important to avoid picking up any other disturbance from the electromagnetic environment. If a gas ionization chamber is used, the charge produced per kiloelectronvolt of particle energy can be more than a factor of 6 lower than in a silicon detector, and electronic noise becomes more important by this same factor. If capacitive noise from the preamplifier is the limiting contribution to the resolution, the performance can be improved by reducing the capacitance of the detector and connecting cable and by using a preamplifier with a cooled field-effect transistor (FET). If the specified noise level (measured by a precision pulser) is not obtained, periodic noise is most certainly involved. Additional information can be found in Goulding and Landis (1982), Radeka (1988), and Morrison (2007).

Tracking and removing periodic noise can be very tedious, and there is no single recipe that reliably leads to success. Basically, there are two strategies for doing so: on one hand, removing the sources of noise and, on the other hand, improving the shielding and reducing the sensitivity of the detector chain against the disturbance. In the following list, we describe tests that can be done and measures that can be taken in pursuing both of these strategies. It has to be mentioned that some actions that improve conditions in one situation might be detrimental in another, depending on the electrical grounding scheme used and the nature of the noise source.

- Check cable shieldings and connectors; the ground lead of the preamplifier input connector especially has to be firm (check by careful twisting). Do not use unnecessarily long cables.
- Beamlines and vacuum vessels are not necessarily good conductors and on a well-defined ground potential. Try to connect the flange that carries the electrical feedthrough to the detector with a solid copper cable to the electrical ground of the detector electronics.
- Extra ground cables have to be of large cross section (10 mm^2 rather than 1 mm^2) and connected firmly. If other cables carry ground along the same line, avoid producing ground loops by slightly twisting cables around each other.
- If you have three-phase electrical power in the laboratory that is split into three two-phase current networks, never mix phases for one experimental setup. Acquisition electronics (including data-collecting computers) should be powered by the same phase. If necessary, install an extra power cable to the computer or control room.
- If possible, try “star grounding” of your electronics to avoid ground loops; that is, use only one single connection to ground potential in the whole system. In this case, the shielding of the detector cable has to be insulated from the vacuum vessel.
- Avoid strong high-frequency emitters close to the experiment. These are often chopped power supplies, turbopump controllers, PC monitors, and so on. If emitters are inside the vacuum vessel (for example, turbopumps), the detector can act as an antenna: rethink the shielding scheme.

- To track the sources of periodic noise, run a fast Fourier transform on an oscilloscope. In some cases, a simple ferrite filter can help.
- Microphonic noise (i.e., mechanical vibrations of the detector) can produce similar disturbances. If produced by a turbopump, it can even have the same frequency as the noise induced by the electromagnetic field.

15.3 CALIBRATION OF FIXED PARAMETERS

In Eq. (15.1), the unknown experimental parameter is the product of the charge Q and the solid angle Ω. The measurement of charge was treated in Section 15.2.1. In Eq. (15.2), the electronics gain Δ appears, as well as the product of the charge and the solid angle, QΩ. In both equations, the scattering angle θ is implicit in both the scattering cross section σ′ and the integration path lengths. This section treats the separate determinations of Ω, Δ, and θ, which are (usually) fixed in any one run.

Solid angle is troublesome to measure accurately at the 1% level, as is routine charge collection in RBS systems, and analysts have used standard (certified) samples for decades to avoid routine use of absolute values of charge and solid angle. It is difficult to determine the detector-to-target distance with a precision of 1% (generating a 2% uncertainty in the solid angle). It should be noted that, if the product of the charge and the solid angle is calibrated on one beam, then care should be taken that no relative error is introduced through current integration when performing an experiment in the same geometry with a different beam. The comments on determination of the solid angle apply to particle detectors, where the intrinsic detector efficiency is known to be 100% for energies exceeding ~30 keV. For γ-ray and neutron measurements, it is more difficult to achieve an accuracy of ~1% for the overall detection efficiency.

15.3.1 Energy

Accelerator energy calibration is critical for accurate work. Clear pitfalls here were highlighted in the first edition of the handbook (also see Section 15.3.2), which pointed out that the first RBS round-robin experiment had very disappointing results partly because of very poor energy calibration (see Section 15.3.2.4). For RBS, the spectra have similar shapes for all energies. Of course, the energy loss is sensitive to the beam energy, but it is not nearly well enough known for use in energy calibration. In any case, the energy loss for any given layer can rarely be measured with a precision exceeding 1%. However, because the cross section is proportional to $1/E^2$ but linear in gain, an energy error will propagate through to errors in the determined layer thicknesses. For elastic (non-Rutherford) backscattering spectrometry (EBS) [and nuclear reaction analysis (NRA)], there are very often strong resonances that, in some circumstances, can lead to very large errors consequent on an energy calibration error. PIXE is the one case where energy is a second-order effect, and one often finds that PIXE laboratories are rather cavalier about energy calibration. This is a potentially serious pitfall for those laboratories if they try to do a more complete analysis using simultaneous particle scattering, as is now desirable with the new codes that handle these multiple techniques self-consistently (such as the DataFurnace code).

One might think that, because all accelerators have resistor chains to distribute the terminal potential down the accelerator column through the column current, the terminal potential could be easily determined through Ohm's law, because the resistors have fixed values. However, these resistors have extraordinarily high values (typically ~10 GΩ) and operate at very high voltages (typically ~40 keV), and high-value high-voltage resistors are known to follow Ohm's law only approximately and, in any case, not reproducibly at the sub-1% level.

Therefore, it is necessary to calibrate indirectly, using established standards (see Tables 15.2 and 15.3). The two primary accelerator energy calibration points are the $^{27}Al(p,\gamma)^{28}Si$ reaction at 991.90

± 0.04 keV and the threshold of the ^{7}Li(p,n)^{7}Be reaction at 1880.60 ± 0.07 keV. These values were taken from the authoritative work of Marion (1966) and are still the currently accepted values [but note the more precise value from White *et al.* (1985) for the latter]. The previous edition of this handbook also included a table of accelerator calibration energies (Tesmer and Nastasi, 1995; Table A19.1, Appendix 19), but it should be made clear that many of those energies were provided for convenience only, are not the accepted values, and should not be used in critical work. For example, the previous edition of this handbook listed a resonance energy of 3035.9 ± 2.3 keV for the ^{16}O(α,α)^{16}O reaction, but the IAEA-recommended evaluated cross-section code SigmaCalc (2009; also see IBANDL, 2009) gives a resonance energy of 3044 keV.

Secondary calibration points can frequently be used to verify the reproducibility of the accelerator energy, usually at a lower precision and almost always at a lower absolute accuracy. EBS resonances are very convenient for this purpose, especially given that there are a number of resonances at high energies and for ^{4}He beams. See Table 15.4 for suggestions, but note that the energy positions of the resonances do not (usually) have an evaluated uncertainty, even though the SigmaCalc cross sections are evaluated. The exception to this is the C(p,p) reaction, for which the energy is very well known. The estimated uncertainties were taken from the original cross-section measurements. To make best use of these resonance energies, considering that the line shapes can be strongly skewed, one of the IBA codes that can handle EBS correctly should be used to fit the spectra obtained. Very high precision can be obtained if the IBA codes are used carefully, even with the very wide resonances.

Table 15.2. Primary (recommended) accelerator calibration points for protons [from Marion (1966), except where otherwise stated]. Note that, for threshhold reactions, the 2003 masses are used (Audi *et al*., 2003); also see the convenient calculator at www.nndc.bnl.gov/qcalc.

Energy (keV)	Reaction	fwhm (keV)	Comment
340.46 ± 0.04	^{19}F(p,αγ)^{16}O	2.4	
872.11 ± 0.02	^{19}F(p,αγ)^{16}O	4.7	
991.90 ± 0.04	^{27}Al(p,γ)^{28}Si	0.1	
1747.6 ± 0.9	^{13}C(p,γ)^{14}N	0.8	
1880.60 ± 0.07*	^{7}Li(p,n)^{7}Be		Marion, 1966
1880.443 ± 0.020*	^{7}Li(p,n)^{7}Be		White *et al.*, 1985
1880.356 ± 0.081	^{7}Li(p,n)^{7}Be		
3235.48 ± 0.29	^{13}C(p,n)^{13}N		
4234.43 ± 0.31	^{19}F(p,n)^{19}Ne		
5796.9 ± 3.8*	^{27}Al(p,n)^{27}Si		Marion, 1966
5803.73 ± 0.12*	^{27}Al(p,n)^{27}Si		White *et al.*, 1985
5803.621 ± 0.100	^{27}Al(p,n)^{27}Si		
6460.47 ± 0.15	^{34}S(p,n)^{34}Cl		
7026.56 ± 1.6	^{60}Ni(p,n)^{60}Cu		
9193.85 ± 0.20	^{54}Fe(p,n)^{54}C		
9510.55 ± 1.46	^{58}Ni(p,n)^{58}Cu		
12728 ± 10	^{16}O(p,p)^{16}O	<2	
14233 ± 8	^{12}C(p,p)^{12}C	<1	
14230.75 ± 0.02	^{12}C(p,p)^{12}C	1.2	Huenges *et al.*, 1973
19641.9 ± 1.1	^{12}C(p,n)^{12}N		

*Both 1966 and 1984 values given for comparison.

Table 15.3. Accelerator calibration points from He threshold reactions. Note that 2003 masses are used (Audi *et al*., 2003), unless otherwise stated; see the convenient calculator at www.nndc.bnl.gov/qcalc

Energy (keV)	Reaction	Comment
1436.7 ± 0.5	$^{12}C(^{3}He,n)^{14}O$	Experimental (two measurements; Marion, 1966)
1437.9 ± 0.6	$^{12}C(^{3}He,n)^{14}O$	Roush *et al.*, 1970
1436.6 ± 0.5	$^{12}C\ (^{3}He,n)^{14}O$	Theoretical (Mattauch *et al.*, 1965)
1435.82 ± 0.14	$^{12}C(^{3}He,n)^{14}O$	Theoretical
2966.1 ± 1.7	$^{6}Li(^{3}He,n)^{8}B$	Experimental (one measurement; Marion, 1966)
2965.0 ± 1.5	$^{6}Li(^{3}He,n)^{8}B$	Theoretical (Mattauch *et al.*, 1965)
2964.9 ± 1.5	$^{6}Li(^{3}He,n)^{8}B$	Theoretical
3796.54 ± 0.33	$^{16}O(^{3}He,n)^{18}Ne$	Theoretical
4380.035 ± 0.612	$^{7}Li(\alpha,n)^{10}B$	Theoretical
6088.04 ± 0.32	$^{14}N(\alpha,n)^{17}F$	Theoretical
6620.54 ± 1.6	$^{6}Li(\alpha,n)^{8}B$	Theoretical
8131.37 ± 0.67	$^{15}N(\alpha,n)^{18}F$	Theoretical
11337.86 ± 0.67	$^{12}C(\alpha,n)^{15}O$	Theoretical
15171.49 ± 0.36	$^{16}O(\alpha,n)^{19}Ne$	Theoretical

Table 15.4. Secondary energy calibration points based on SigmaCalc, version 1.6. Note that uncertainties were derived from the original literature, not from SigmaCalc, and are standard deviations, not fwhm.

Energy (keV)	Reaction	fwhm (keV)	Reference
3044 ± 5	$^{16}O(\alpha,\alpha)^{16}O$	10	SigmaCalc (unpublished to date)
3885 ± 5	$^{16}O(\alpha,\alpha)^{16}O$	2	SigmaCalc (unpublished to date)
4265 ± 5	$^{12}C(\alpha,\alpha)^{12}C$	27	Gurbich (2000)
3470	$^{16}O(p,p)^{16}O$	2	Gurbich (1997)
1483	$^{24}Mg(p,p)^{24}Mg$	0.3	Gurbich and Jeynes (2007)
1748.5	$^{14}N(p,p)^{14}N$	9	Gurbich (2008)
3198	$^{14}N(p,p)^{14}N$	6	Gurbich (2008)
1734 ± 0.2	$^{12}C(p,p)^{12}C$	45	Gurbich (1998)

A competent operator should be able to obtain a terminal voltage calibration at an absolute accuracy better than 0.1%, but this is not easy, partly because this level of accuracy is never easy to achieve, partly because precision at this level is usually limited by counting statistics (so that significant beam time is required), and partly because such accuracy requires careful attention to the quality of the sample surface used. An aluminium sample should be well polished (shiny) and clean, and a lithium sample (which is very reactive) should have a fresh surface prepared each time *in situ* by being cut with a knife under an argon atmosphere. Bear in mind that one needs only a 13-nm (5 $\mu g/cm^2$) alumina layer or a 4 $\mu g/cm^2$ carbon layer to give a 1 keV energy loss for protons at 1 MeV.

Moreover, many modern accelerators are tandem machines, where a 0.1% uncertainty in the terminal voltage translates into a 0.2% uncertainty in the beam energy. Analysts should not forget that there is also the injection voltage of the ion source into the accelerator, which is a voltage additional to the terminal voltage, so that, when the linearity of the accelerator is determined, there should always be a zero offset (of the right sign!) equal to the injection voltage. Of course, this ~20 kV injection voltage can (and should) be measured directly with readily available instruments.

The good news is that generating voltmeters (GVMs), the instruments that monitor the terminal voltage) are usually both very stable and astonishingly precise. Modern tandem machines have GVMs that are reproducible and stable over months at the 0.05% level. However, the GVM is a variable-capacitance device that uses the induced ac voltage as a monitor for the terminal voltage. The voltage induced on the GVM is directly proportional to its distance from the terminal and is therefore subject to a temperature coefficient, which, for example, is 0.03/°C on the Surrey HVEE 2 MV Tandetron. For accurate work using energy feedback based on a GVM, the accelerator hall temperature must be closely controlled.

15.3.2 Solid angle

In this section, we consider the determination of solid angle, one of the critical parameters in Eqs. (15.1) and (15.2). It is mostly determined indirectly using a standard, and we consider first NRA standards and then various RBS standards.

Whenever the cross section varies significantly across the finite solid angle of the detector, as is the case for many nuclear reactions, as well as for non-Rutherford elastic scattering, care must be used to properly integrate over the solid angle with respect to the angular dependence of the cross section. Care should also be taken (especially for higher-energy incident beams, which can give rise to unexpected nuclear reactions) in choosing an aperture that is opaque not only to megaelectronvolt α-particles but also to more penetrating particles, such as high-energy protons.

If there is an accurately calibrated radioactive source of small area (for example, ^{241}Am), then the solid angle can be determined directly by placing the source at the position of the target. However, it is usually difficult to reduce the uncertainty in positioning the α -source to the desired 1–2% level.

15.3.2.1 NRA standards

In discussing reference standards, we are also talking about those nuclear reactions for which the corresponding cross sections are well known at the level of a few percent. To date, probably the most widely used standard for NRA applications has been that for ^{16}O, specifically anodically grown thin Ta_2O_5 targets on a Ta substrate. The Paris group (Amsel and Samuel, 1967) pioneered their use through the $^{16}O(d,p_1)^{17}O$ reaction at a bombarding energy of 972 keV and a detector angle assumed to be 150° but more likely to be 164°. Here, there is a broad (–85 keV) resonance in the reaction cross section. The protons are emitted with an energy of 1.6 MeV, and the cross section has been measured with a precision of ±3% by Davies and Norton (1980) to have a value of 13.3 mb/sr and by Lennard *et al.* (1989) to have a value of 13.6 mb/sr. Seah *et al.* (1988) reported a successful round-robin intercomparison of absolute measurements in different laboratories using this reaction. Gurbich & Molodtsov (2004) reported the excitation function for this reaction at 150°.

For those not having access to deuterium beams, substitution of ^{18}O in the electrolyte allows $Ta_2{}^{18}O_5$ targets to be fabricated. The $^{18}O(p,\alpha)^{15}N$ reaction at E = 750 keV could then be used, although the cross-section value is not known as well as for the $^{16}O(d,p_1)^{17}O$ reaction (Christensen *et al.*, 1990). The $^{16}O(^3He,a)^{15}O$ and $^{16}O(^3He,p)^{18}F$ reactions are also useful, and some cross-section values have been reported (Lennard *et al.*, 1989; Abel *et al.*, 1990). It should be noted that oxygen from a Ta_2O_5 oxide layer will begin dissolving back into the Ta substrate at a temperature of ~700 K (Smyth, 1966). Indifference to beam heating of standards is therefore not encouraged.

The cross section for the $^3He(d,p)^4He$ reaction (Q value of 18353 keV) is very well known (±2%) for a center-of-mass energy of 250 keV (σ_{lab} = 58 mb/sr) (Davies and Norton, 1980; Möller and Besenbacher, 1980). Unfortunately, ^{3}He targets fabricated by ion implantation are sometimes not stable under prolonged ion beam bombardment (Alexander *et al.*, 1984; Geissel *et al.*, 1984).

15.3.2.2 Hydrogen isotope standards

Stable hydride or polymer targets suitable for hydrogen (or deuterium) thin-film standards are still few. There are problems in the preparation of reference targets by ion implantation (current integration, dose uniformity, depth profiles, and stability: see Amsel and Davies, 1983).

Recently, Banks *et al.* (2004) showed that standard samples could be made from hydrides of Er and that these samples were stable to ^{4}He beams, but the samples were both rather rough and rather thick, needing >5 MeV ^{4}He to look all through them with elastic recoil detection [ERD; also called elastic recoil detection analysis (ERDA) and forward recoil spectrometry (FRES or FRS)]. However, an absolute H (and D) content was determined independently of IBA to better than 2%, and ERD and NRA have an uncertainty of 3.3%. Boudreault *et al.* (2004b) reported an interlaboratory reproducibility for H implanted in Si at 2.2%, although the expanded uncertainty (k = 1) was estimated at 6%.

15.3.2.3 BAM hydrogen standard

Reinholz *et al.* (2008) established a hydrogenated amorphous silicon (a-Si:H) certified reference material (CRM) grown by chemical vapor deposition (CVD) with about 10 at. % H in a 1–2-μm-thick a-Si layer (on a Si substrate) with an expanded uncertainty (k = 2) in the H content of about 1% (BAM, 2009).

15.3.2.4 Bi-implanted (Harwell) standard

In 1975, an RBS round-robin experiment was conducted to test whether the often-claimed ±2% accuracy was actually being achieved. Several Si wafers were implanted at the UK Atomic Energy Agency (UKAEA, Harwell site) with ~5×10^{15} Bi/cm^2 at an energy of 40 keV, which locates the Bi distribution at a depth of ~20 nm. These samples, which became known as the Harwell Series I standards, were then partitioned into 1-cm^2 pieces and distributed to ~50 RBS laboratories around the world. The results, reported by Baglin at the 1975 Karlsruhe IBA conference, were disappointing. Even among experienced laboratories, discrepancies of ±20% were common, and some results varied by 50% or more. The individual causes were never fully resolved, but from the shape of the 1.9 MeV H^+ RBS spectra (including the strong 1.6 MeV resonance in Si), Baglin concluded that several laboratories did not even have a correctly calibrated accelerator energy scale.

Subsequently, a collaboration between ion beam groups at Chalk River (Ontario, Canada), l'Université de Paris, Harwell, and Geel (Belgium) developed several independent methods of calibrating the Bi content of the Harwell standards, eventually obtaining very satisfactory (±2% or better) agreement among the different laboratories (Cohen *et al.*, 1983). In the course of these studies, several of the pitfalls noted in this chapter became recognized for the first time. For example, the energy dependence of the Bi yield was observed to deviate slightly from the expected $1/E^2$ Rutherford law, and this observation led to the recognition of the electron screening correction. Many pitfalls associated with poor Faraday cup techniques were identified and corrected. Also, the problem of charge exchange along the beamline was found to be responsible for significant fluctuations (±4%) in some of the Harwell Series II Bi implantations (Davies *et al.*, 1986).

The resulting comparison, with the same Bi-implanted wafer being used in all three laboratories, showed a ±2% agreement and therefore demonstrated that RBS can achieve the expected absolute accuracy without the use of any calibrated standard. In practice, because the detector solid angle and the scattering angle are difficult quantities to measure accurately, it is simpler to use a previously calibrated standard instead.

Harwell Series I wafers have a Bi content of 4.87 (±0.08) × 10^{15} Bi/cm^2 (Wätjen and Bax, 1994). Series II wafers have the same nominal Bi content as Series I, but fluctuations as large as ±4% have been found (as noted above). Hence, whenever greater accuracy is required, one should obtain a wafer that has been cross-calibrated against a Series I standard. These samples can still be found; however, they have now been superceded by the a-Si standard, which is readily made, and also by the much more accurate Sb-implanted standard. These new standards are described in the next two subsections.

15.3.2.5 BAM/IRMM Sb standard

Sb-implanted samples are available from the Institute for Reference Materials and Measurements (IRMM), Geel, Belgium, and the Bundesanstalt für Materialforschung und -prüfung (BAM), Berlin, Germany, and are certified at 0.6% (registered as IRMM-302/BAM-L001: Pritzkow *et al.*, 2001; Ecker *et al.*, 2002). These samples supercede the Harwell Bi implant samples, but are used in exactly the same way.

The samples are an implant of Sb into Si with a range of 160 nm and a certified Sb fluence of 48.1 (± 0.3) $\times 10^{15}$/cm^2 (1σ uncertainty). The Si wafer has a 90-nm oxide (of uncertified thickness). This standard has been used once to date in published work for a traceable RBS analysis of some As implants (Boudreault *et al.*, 2004a), and it has also been used to validate Si stopping powers (see next subsection). In both of these applications, the Sb standard was transferred through the a-Si substrate yield, and to do this more accurately, the Sb standard was amorphized to a depth of 630 nm with a cold 500 keV Si self-implant of 5×10^{15}/cm^2 fluence.

15.3.2.6 a-Si standard

Useful work has been done on new standard samples involving measurement of the surface yield of an implanted (amorphized) silicon sample (Lennard *et al.*, 1999; Bianconi *et al.*, 2000). This is nearly equivalent to an absolute measurement of the energy loss of ^{4}He in Si if a series of measurements are made at different energies. Konac *et al.* (1998) made direct measurements of the energy loss of ^{4}He in Si (also known as the inelastic electronic energy-loss cross sections or the stopping power) with an uncertainty of about 2% (these important measurements are often referred to in the literature as KKKNS), and Niemann *et al.* (1996) also made measurements of energy loss in Si with an uncertainty approaching 1%. The stopping-power function was systematically extracted using Bayesian methods, along with uncertainty estimates, from the measurements of Bianconi *et al.* by Barradas *et al.* (2002).

In their study, Bianconi *et al.* (2000) made absolute measurements of the product of the charge and solid angle, at nominally 1% accuracy, and obtained agreement within the stated error. The traceability of Lennard *et al.*'s (1999) work is not as easy to establish, but they obtained the same values and consistency with KKKNS. The conclusion of all of this work is that the measured Si stopping cross sections have an uncertainty (1σ) of 2%.

We should highlight the fact that the Si stopping powers stored in the SRIM-2003 database (Ziegler, 2004) were used to determine the Sb content of an IRMM-certified Sb sample (see previous subsection) for 1.5 MeV He RBS, and it was found that the certified value was obtained within 0.3% (with a 1σ uncertainty of 0.2%) (Barradas *et al.*, 2007, 2008). This demonstrates that, for this He beam energy, the SRIM-2003 stopping powers for Si are correct to within the 1σ uncertainty of the certified sample: 0.6%.

The point to emphasize here is that Bi or Sb implant samples are specific artifacts, but every laboratory can make its own amorphized Si samples on demand. Secondary standards must be used systematically with the Bi or Sb certified standards, along with the associated error and complexity; not so for the amorphized Si. The difficulty with certifying the Bi implants has been in establishing the real variation across the implant batch, but the uniformity and purity of modern production silicon ingots has been established at extraordinary sensitivity and accuracy: modern standard RBS samples can now take advantage of this fact.

15.3.3 Electronic gain

It is harder than generally supposed to establish the electronics energy calibration (the gain, in keV/channel) with an accuracy better than 1%, and it is easy to make errors of 2% and more. Whenever a spectral area is being evaluated [Eq. (15.1)], only the product of the charge and solid angle, $Q\Omega$, is required (this is the case when using the Bi or Sb standards), but if the a-Si yield (or

other stopping power) is being used to calibrate the solid angle, then Eq. (15.2) is invoked, which uses the product $Q\Omega\Delta$, and the gain is also required to evaluate the product $Q\Omega$ needed for interpreting spectral areas. The Si stopping powers have been compared directly with the Sb standard and are therefore very accurately known (for 1.5 MeV He); other stopping powers are not usually known to much better than 4%. Nevertheless, it is a bad analytical mistake to omit the determination of one of the local parameters of the analysis because there might be a systematic error in one of the global parameters. After all, the stopping powers of a material are constant, even if they are not known very well, but the analysis is not repeatable if the local parameters are not accurately determined. In this section, we therefore dwell on the determination of the important gain parameter Δ at some length.

To determine the gain, one must find a sample that has several (at least two!) elements of both high and low Z at the surface. We consider a Au/Ni/SiO_2/Si sample (Fig. 15.4) (Jeynes *et al.*, 1998), where the Au and Ni films are 15 TFU thick and the oxide is 1500 TFU thick [1 TFU (thin film unit) = 10^{15} atoms/cm^2; see Section 15.7.3]. The Ni film is used to wet the oxide for the Au deposition, and this sample has excellent long-term stability. For this sample, the Si and O "surface" signals are actually buried under the metal layers, and an accurate calibration must take this fact into account.

This discussion will be in terms of the above-described sample, and the reader can substitute his own favorite calibration sample. Consider the following examples of what is possible: In the very careful work of Bianconi *et al.* (2000), a seven-point calibration was used, with a Type A estimate of 0.2% uncertainty (see Section 15.5.1) (this estimate was published in Barradas *et al.*, 2007). Munnik *et al.* (1996) described stopping-power measurements using RBS with an uncertainty on the gain of 0.16%. Gurbich and Jeynes (2007) determined the gain with a Type A uncertainty of <0.1%.

To determine the gain, we have to identify channel numbers corresponding to well-known energies and then do a linear correlation to obtain the gain (Δ) and offset (o) values: $E_c = \Delta C + o$, that is, the energy E_c is represented by a particular channel C. The surface signal of element E is given by $E_e = k_e E_0$, where E_0 is the incident beam energy and k_e is the kinematic factor for element E. The kinematic factor is known analytically of course and depends (fairly weakly at large angles) on the scattering angle θ. Thus, for an accurate gain calibration, both the beam energy and the scattering angle must be known rather precisely. This discussion ignores the pulse height defect (see Section 15.3.3.4).

15.3.3.1 Fractional channel numbers

To identify the channel numbers, the user chooses the signal peak for very thin layers and the signal half-height for thick layers. For an accurate gain determination, it is essential to find the channels as real numbers, not as integers. The reader might demur here, saying that the detector resolution is (typically) 16 keV and the channel width is only (say) 3 keV/channel, so we are demanding an unphysical precision. However, the reader should remember that, first, in accurate work, one should always use one or more significant figures than is justified by the intrinsic experimental precision, to avoid rounding errors, and, second, some parameters of the data can be established with a precision much greater than the nominal system resolution. This latter point was made very strongly by Jeynes and Kimber (1985), who showed that the peak of a distribution in an RBS spectrum can be determined with a precision of about 300 eV where the detector resolution is 15 keV.

It is therefore clear that the best gain determination will not be made unless numerical methods are used to determine real (fractional) channel numbers precisely. This is, incidentally, the only reason for using ADCs at high resolution for collecting relatively low-resolution RBS spectra: In Fig. 15.4, we show 512-channel spectra, but we could easily use 4000 spectra, in which case integer channel numbers would be at sufficient resolution for determining the gain as precisely as is possible.

However, standard theory (the Nyquist theorem) says that sampling at greater than 3 times the resolution gains no extra information, so strictly speaking, 4000 spectra are a waste of space!

15.3.3.2 Correlated gain and offset

The IBA codes all have facilities for fitting spectra to extract the electronic gain. Of course, it is necessary to determine both the gain and the offset, even though the value of the offset has no importance and the gain and offset are strongly correlated. Therefore, an error in the offset gives a corresponding error in the gain. This is why it is so easy to have large errors in the gain. The fitting used by the codes might not handle this correlation correctly, giving the user a false estimate of the true accuracy.

15.3.3.3 Detector resolution

Fitting codes usually use some sort of χ^2 function to obtain minimum values. Because the positions of edges and peaks can be determined with extraordinary accuracy from RBS spectra, RBS is very sensitive to the effect of the detector resolution on the widths of these edges or peaks. Therefore, the analyst often finds that noticeably different results are obtained when the detector resolution is not correctly determined (see Section 15.3.6 below).

15.3.3.4 Pulse height defect

Although the accelerator energy can be established readily at about 0.1%, the absolute electronics calibration depends on an accurate knowledge of the pulse height defect of the detector. Semiconductor radiation detectors are known to respond in a nonlinear fashion to particle energy. Normally, the deviations are lumped into the so-called pulse height defect (PHD), which includes the effects of the detector entrance window and dead layer, as well as the nuclear (nonionizing) energy loss of the projectile arising from elastic collisions with the atomic lattice of the detector material.

The preceding discussion ignored this effect, treating the energies of the surface signals as being given only by the kinematics. However, in reality, the detector sees only that fraction of the energy of the particle that is deposited into electron–hole pairs (that is, after passing through the entrance window and dead layer) and for which the electrons do actually reach the detector anode and are not lost in recombination sites (defects). Old detectors could have significant radiation damage, providing a significant number of recombination sites. These detectors will no longer behave linearly and cannot be used for accurate work, although all IBA codes allow nonlinear gains to be used.

However, all detectors, even high-quality (new) ones, will detect a particle energy significantly less than the particle has when leaving the sample, as a result of the PHD. Usually, this effect can be ignored because the absolute value of the correction is small. For instance, Bianconi *et al.*'s (2000) high-precision gain determination referred to in Section 15.3.3 did not correct for the PHD, but this introduced an error of only 0.2% (Barradas *et al.*, 2007, 2008). Moreover, the nonlinearity in the detector response that must exist because the PHD varies with particle energy is so small that it cannot be detected in standard cases (Jeynes *et al.*, 1998), being mimicked by a (slightly different) linear gain. However, in cases where different spectra collected at significantly different beam energies must be compared, it is essential to apply the PHD correction for the best accuracy.

The PHD was comprehensively described by Lennard and Massoumi (1990), and Jeynes *et al.* (1998) presented a full (manual) analysis in a particular case where the best demonstrable accuracy for the electronic gain, Δ, was only 0.5%. Lennard *et al.* (1999) did not make a comparable accuracy estimate explicitly, but their work is also consistent with an accuracy in Δ of about 0.5%. The extremely accurate analysis of Munnik *et al.* (1996) includes a full PHD correction, and Gurbich and Jeynes' (2007) benchmark measurement of the ^{nat}Mg(p,p)^{nat}Mg elastic scattering cross sections depends on the analysis of a PHD-corrected set of spectra with a single gain across the whole energy range (see Fig. 15.3 for one of these spectra).

A further effect that has been studied in some detail (Lennard *et al.*, 1986; Bauer and Bortels, 1990; Comedi and Davies, 1992) in Si for light ions (^{1,2}H, ^{3,4}He, ^{7}Li) arises as a consequence of the differing ionization densities produced by the incident particles. In principle, an IBA spectrum can easily be obtained using higher-energy beams for which various nuclear reactions occur and various types of particle all enter the detector; for such a spectrum, one could perhaps use a single absolute electronics calibration if the PHD correction could be done correctly. However, no PHD-corrected data have yet been published for these types of NRA spectra that also correct for the particle type, although Pascual-Izarra and Barradas (2008) describe a full PHD correction in detail.

15.3.4 Scattering angle

The scattering angle, θ, is the angle the detector makes with the incident beam. This should be measured as accurately as possible because, even at $\theta = 150°$ and normal beam incidence, an uncertainty of only 0.2° gives an uncertainty of 0.3% in fluence measurements (see Section 15.5). For glancing-beam exit geometries, any uncertainty in the scattering angle greatly amplifies the uncertainty of the results.

Where a goniometer is used (presumably including most applications of glancing exit geometries), it is easy to measure scattering angle: One only has to shine a laser down the beam path and reflect it onto the detector from a mirror at the sample position. The scattering angle can then be read from the goniometer. Care must be taken in precision work to specify the plane of the sample because this affects the scattering angle. For small detectors, the blocking effect in single crystals can also be used to detect the scattering angle. In this method, one aligns a major axis of the crystal with the detector (not the beam), looking for a dip in the yield. The beam energy has to be such that the detector solid angle is not too much larger than the channeling critical angle.

In some cases, the angle subtended by the detector has a significant effect on the result. For glancing-beam-exit work, the detector must be collimated in one direction to restrict the possible variation in scattered-particle exit path length to the detector. For these geometries, it is worth noting that curved collimation slits are optimal (Brice and Doyle, 1990). For some elastic (non-Rutherford) backscattering (EBS) reactions, the cross section varies strongly (and nonlinearly) with scattering angle, and for larger detectors, the average scattering angle might not accurately represent the data. This is actually another good way to determine true effective scattering angles. For example, for the 1735 keV resonance in the ^{12}C(p,p)^{12}C EBS reaction, the maximum cross section relative to the Rutherford value for 150° is 39.06, but for 150.2°, it is 39.34, a change of nearly 1%. Conversely, if EBS resonances are being used to analyze light elements, the actual angles must be verified for accurate work.

15.3.5 Detector resolution

We already noted (Section 15.3.3.3) that fitting programs are sensitive to the value used for detector resolution because the shapes of edges and peaks are determined very precisely in RBS spectra. Figure 15.4 shows a Au/Ni/SiO_2/Si calibration sample spectrum with fits assuming various detector resolutions. The signals from the thin metal surface layers have a shape entirely determined by the detector resolution. To determine the detector resolution, the height of the signals must be matched, given that the signal area is also matched. The fitted gain is given in all cases in Fig. 15.4, given that the metal thickness is fixed. A 4% change in resolution gives a maximum 0.25% change in gain. The fact that the gain can be affected at all by the resolution, albeit at second order, is surprising at first sight.

Also shown is the fitted metal thickness: In this case, a 4% change in the resolution gives a 1.5% change in the fitted thickness. This is almost a first-order effect even though one might have thought that there should be no change. The size of this sort of effect depends strongly on how the fitting algorithm (in this case, a grid-search χ^2 approach) works, and the reader should be warned that fitting algorithms do not always behave as one might intuitively expect.

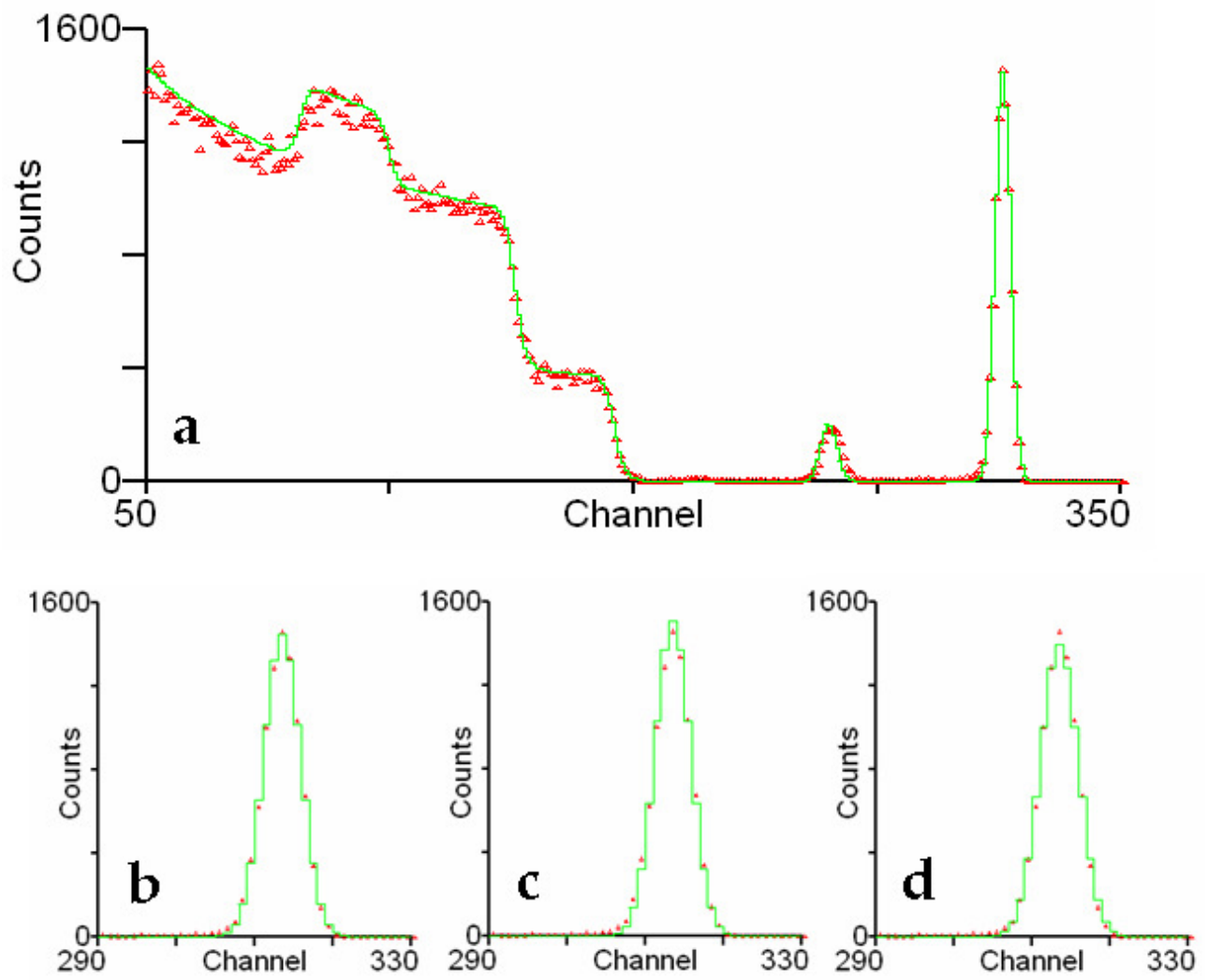

FIG. 15.4. Detector resolution and its effect on the calibration of gain. (a) Spectrum for 1.557 MeV $^4He^+$ RBS with scattering at 149.2°. Sample is Au/Ni/SiO_2/Si (12.8/14.8/1607 TFU). (b) Detector resolution of 25 keV, fitted gain for fixed metal thickness = 4.457 keV/channel (fitted metal thickness = 28.55 TFU); (c) 24 keV, 4.472 keV/channel (28.07 TFU); (d) 26 keV, 4.460 keV/channel (28.96 TFU).

In principle, the detector resolution function is neither Gaussian nor even symmetrical, and in the most accurate work, it is necessary to account for this aspect in detail. This should be done as a matter of course for PIXE, where the detectors have relatively high resolutions (typically <200 eV) and the shape of the instrumental function is well-known to be non-Gaussian. The GUPIX program (see Blaauw *et al.*, 2002), for instance, assumes that the instrumental function is specified in detail by the user. For PIXE, the instrumental function must be measured as a function of X-ray energy over the whole energy range using a series of pure targets. If this is not done, the ratios of the various K and L lines cannot be determined with precision. Particle scattering detectors have much lower energy resolution (typically ~15 keV), and the instrumental functions of these detectors are not usually measured in detail, although remarkable results can be obtained when it is. Fischer *et al.* (1997), for example, demonstrated that they could reliably resolve the isotopes of Co using a full Bayesian deconvolution code! However, none of the routine IBA codes currently have facilities for a particle scattering detector resolution that is a function of energy, and the highest-resolution work yet reported with these detectors (determining interface roughness of <1 nm) used a simple Gaussian (symmetrical) function (Barradas, 2002).

However, in general, the lesson is that, for accurate work, all of the parameters should be correct.

15.4 ALGORITHMIC ISSUES

In this section, we consider a number of issues that affect the interpretation of spectra and provide occasion for various subtle pitfalls for the unwary. To perform a traceable analysis, one must be able to accurately estimate the parameters in Eqs. (15.1) and (15.2) (considered in turn in the preceding section), but one must also be able to accurately do the integrations implicit in these equations. Here, we consider how well-known the Rutherford (and non-Rutherford) elastic scattering cross sections and the inelastic electronic stopping cross sections are. We also discuss the limits within which the basic single-scattering assumption is valid and how well the user can calculate the variation of the energy resolution with depth.

15.4.1 The Rutherford cross section

How accurate is the Rutherford scattering law? This is often the key question in achieving quantitative RBS analysis, because its main advantage is the assumed existence of a universal and predictable scattering cross section, σ_R (cm^2/sr), whose dependence on beam energy E (MeV), scattering angle θ, and atomic numbers Z_1 and Z_2 of the beam and target atoms, respectively, can be accurately described by Rutherford's formula obtained from the Coulomb potential (see Chapter 4).

The validity of this point-charge Rutherford scattering law requires the distance of closest approach (collision diameter or impact parameter), b (pm) = $1.44Z_1Z_2$/[E (keV)], between the projectile and target nuclei to fall within the Rutherford window (although note that this window does not really exist: see Gurbich, 2004). This means that b must be considerably larger than the nuclear radius of the target atom [r_n (fm) = $1.4A_2^{1/3}$]. At the same time, b must also be much smaller than the atomic K-shell radius, r_K (pm) = $50Z_2$, in order to minimize electron screening effects. A quick and simple estimate of the upper and lower energy limits within which the scattering cross section should be within ±4% of the σ_R value can be estimated by requiring b to fall in the range $r_K/2 > b > 3r_n$.

Note, however, that a small screening correction to σ_R is always necessary, even though most of the collision is completely unscreened. This arises because the initial part of each scattering trajectory is fully screened (i.e., from ∞ to $50Z_2$ pm from the target nucleus). Consequently, the incident projectile penetrates into the unscreened region with somewhat higher energy than would occur if the target atom were a bare nucleus. The resulting decrease in cross section below σ_R is usually much less than 4%. Furthermore, experimental studies by L'Ecuyer *et al.* (1979), Andersen *et al.* (1980), and Hautala and Luomajarvi (1980) showed that its magnitude is predicted (with reasonable accuracy in most cases) by the relationship

$$\sigma = \sigma_R (1 - 0.049 Z_1 Z_2^{4/3}/E), \tag{15.3}$$

where E is the projectile energy in keV. Strictly speaking, the center-of-mass energy should be inserted into Eq. (15.3), but the screening correction is usually small enough that the use of laboratory coordinates introduces negligible error. This L'Ecuyer *et al.* correction is incorporated in the main IBA codes. The uncertainty in the screening correction is cited as 0.5% by Wätjen and Bax (1994) for the case of 1.5 MeV ^{4}He on Bi, and this uncertainty can be scaled for other cases from Eq. (15.3). However, for small scattering angles or for heavy-ion beams, L'Ecuyer *et al.*'s correction is not as accurate as that proposed by Andersen *et al.*, which takes into account the dependence of screening on the scattering angle. Andersen *et al.*'s correction is also incorporated in the main IBA codes and should be used.

If the energy exceeds the upper limit for RBS, then we are in the regime of non-Rutherford elastic backscattering spectrometry (EBS). As examples, proton scattering on C is significantly non-Rutherford at 380 keV, and He scattering on C is significantly non-Rutherford at 2.2 MeV. The rough estimates above should not be relied on for accurate work; instead measured cross sections should always be used. The IAEA has sponsored a database of EBS cross sections (IBANDL, 2009). The analyst should be aware that these cross sections are a strong function of scattering

angle, so that, if measurements are not available for the angle used, then accurate EBS work cannot be done. However, for some nuclei, the EBS cross sections were evaluated by Gurbich, who determined the quantum mechanical parameters of the nuclear scattering by a fit to all available data for these nuclei using the program SigmaCalc (SigmaCalc, 2009). These cross sections are the most reliable and are valid for (almost) all scattering angles. Both the IBANDL database and the SigmaCalc calculator are under active development, and analysts should check whether cross sections they need are included yet. Where SigmaCalc has cross sections, they should always be used. Note that the IBA codes always give the user access to these cross sections even if they have default values, and the user should know which cross sections are being used by the codes.

If the energy is below the lower limit for RBS, then the major part of the collision takes place before the projectile has penetrated all of the electron shells of the target atom; that is, the unscreened Coulomb field assumed in Rutherford scattering plays a minor part in the collision. With megaelectronvolt accelerators and surface-barrier detectors, this almost never happens, even for the heaviest target nuclei. However, backscattering studies in the medium-energy ion scattering (MEIS) regime involve energies well below the limit for Rutherford scattering. For quantitative work, suitable algorithms are given by Mendenhall and Weller (1991); however, they point out that a fairly accurate (2–3%) approximation to the screened Coulomb cross section can still be obtained by applying the simple screening correction of Eq. (15.3).

15.4.2 Electronic stopping cross sections

Almost all IBA work relies on electronic stopping cross sections. In particular, quantification of depth profiles depends on the stopping-power values used. The same is true of elemental concentrations in most cases.

Different sources of stopping powers are available, from *ab initio* theoretical calculations to experimental data covering a limited energy range of a given ion in a given material. The most widely used source is SRIM (Ziegler, 2004), which is a semiempirical interpolation scheme that covers all ions at all energies in all materials. Users should be aware that SRIM has evolved over the years, and different versions provide different stopping values. The same is true of data analysis codes, where different versions might incorporate different SRIM versions. Other sources of tabulated stopping powers exist and are also used, namely, ICRU (1993) and MSTAR (Paul and Schinner, 2001, 2002) (the latter for heavy ions only).

A statistical analysis performed by Ziegler (2004), including all of the over 25,000 data points in the SRIM-2003 database, showed that the accuracy of SRIM-2003 stopping calculations was 4.2% and 4.1% for H and He ions, respectively. The accuracy was found to be only 5.1% and 6.1% for Li and heavier ions, respectively. However, these values are average estimates and do not represent the uncertainty for any given system. In the same analysis, it was shown that SRIM-2003 predicts around 75% of stopping values within 5% of experimental values for H and He ions, but only 58% for heavy ions. That is, for heavy ions, 42% of the stopping-power values calculated with SRIM-2003 differ from the experimental values by more than 5%. This decreases to 18% for errors larger than 10%. It is worth noting that the experimental measurements for stopping power are notoriously hard to make, so that, even if SRIM reproduces the experimental data, there is no guarantee that the data are correct.

The outcome is that, for H and He ions (and increasingly for Li as well), the tabulated stopping values are normally accurate (at the 5% level), but in some particular systems, large errors can be made. Users interested in high accuracy should check the literature for experimental values and compare them with the calculations. In some systems, highly accurate data are available. On the other hand, for heavier ions, the experimental data are sparse, and the calculations can be inaccurate for many systems. Advances in the accuracy of heavy-ion stopping are continuously being made, so the situation might improve in the coming years. In the meantime, reliance on tabulated, often interpolated, stopping values might be the only practical solution, but it can lead to large errors.

Paul and Schinner (2003, 2006) conducted statistical analyses of the accuracy of stopping powers from different sources, including SRIM-2003 (and older versions of SRIM), ICRU, and MSTAR, for light and heavy ions in solids, gases, and compounds. The main conclusion is that the three sources are equally accurate in most cases, as long as the most recent versions are used.

Great care should be exercised when analyzing compounds, particularly insulators, because most codes use the Bragg rule to calculate the compound stopping from the elemental stopping powers. This approach leads often to larger errors. SRIM-2003 implements the so-called cores-and-bonds (CAB) correction, which is, however, limited to some tabulated compounds. The alternative is to use the molecular stopping powers if available from experiments, which some IBA codes can use.

In all cases, we should emphasize that, when Eq. (15.2) is used, the dominant uncertainty almost always comes from the stopping-power database.

15.4.3 Plural and multiple scattering

One major assumption in most RBS and IBA studies is that the incoming and outgoing trajectories are completely linear, that is, only one significant angular deflection, namely, the Rutherford backscattering event, is occurring. However, the mean free path for unscreened scattering events $[(N\pi a_{TF})^{-1}]$ is only ~100 nm, where N (atoms/cm^3) is the atom density of the target and $a_{TF} \approx 10$ pm is the appropriate Thomas–Fermi screening length (and note that, at megaelectronvolt energies, only unscreened scattering can contribute significantly to the mean deflection angle). Hence, even at quite shallow depths, a fraction of the beam undergoes significant secondary deflections along the incoming/outgoing trajectories. If not taken into account, these secondary deflections can lead to an incorrect interpretation of data.

Full quantitative treatment of such effects requires a Monte Carlo simulation of each particle trajectory. Such calculations have undergone major improvements in terms of accuracy and efficiency (Arstila *et al.*, 2001), but they are still difficult to use in routine work. Some traditional codes now include both multiple and double scattering.

The term plural scattering describes trajectories in which the ion suffers several large-angle scattering events before being detected. A particular case is double scattering, corresponding to two large-angle events. The combined kinematic factor can be larger than the kinematic factor for single scattering, leading to yields above the nominal surface signal energy. The most important effect, however, is an increase in the yield at low energies, along with a low-energy background.

At least two well-known data analysis codes, SIMNRA (Eckstein and Mayer, 1999) and DataFurnace (Barradas, 2004), include the calculation of double scattering in RBS as a user option. Calculation times are much longer than for single scattering. One example is shown in Fig. 15.5, where the SIMNRA simulation matches both the data and a Monte Carlo simulation for 0.5 MeV ^{4}He ions backscattered from about 115 nm of Au on Si at a scattering angle of 165°. A comparable RBS example for DataFurnace shows a TiAlN/Mo multilayer measured at grazing incidence, with a good fit including the effects of a large double scattering signal extending to low energies (Barradas and Jeynes, 2008).

Multiple scattering refers to the succession of many small-angle scattering events, leading to an angular broadening in the beam path. Such secondary deflections obviously change the scattering angle involved in the main RBS collision, thus affecting the magnitudes of both the cross section and the kinematic energy-loss factor. Furthermore, it also affects the depth-to-energy conversion scale.

However, the net effect of multiple scattering is, to first order, an extra contribution to the energy spread of the beam (Szilágyi *et al.*, 1995). This can be the largest contribution to straggling in some situations, particularly in grazing-angle experiments, and it must be taken into account for a correct interpretation of the data.

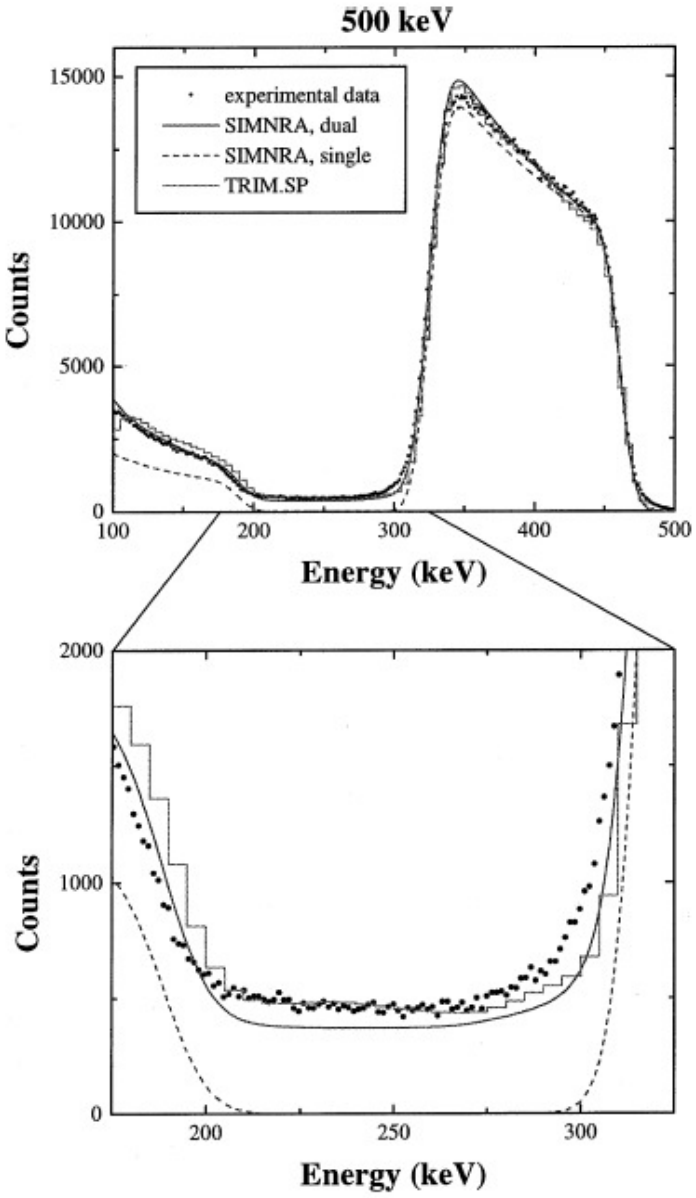

FIG. 15.5: Double scattering effects in ^{4}He RBS of Au on Si. Comparison of the experimental energy spectrum (dots) at a polar emission angle of 15° for 0.5 MeV ^{4}He. The histogram gives the TRIM.SP result; the dashed and solid lines represent the single-collision model and the dual-collision approximation, respectively, both calculated with SIMNRA. The lower part of the figure shows the background between the Si edge and the lower Au edge in more detail. (Reproduced from Eckstein and Mayer, 1999.)

A second effect of multiple scattering is that the shape of the energy spread is no longer Gaussian. This can become important for heavy ions in heavy targets, at low and intermediate energies. Some limited treatment of this effect is included in some IBA codes.

Multiple scattering is very small for light ions at near-normal incidence (and detection). It can be very large for heavy ions or for grazing-angle incidence or detection even for He beams. In that case, whenever depth profiles, roughness, or other sample features that affect the sharpness of signals are studied, the contribution of multiple scattering to straggling must be calculated and included in the analysis.

Note that current versions of a popular computer code for the simulation of RBS profiles, RUMP (Doolittle, 1985, 1986), do not include any treatment of plural or multiple scattering.

15.4.4 Depth resolution

Depth resolution is defined as the minimum separation in depth between two layers such that a maximum in the observed signal is observed for each layer. It determines the capability to separate signals arising from different layers.

In RBS, depth resolution is best near the surface and degrades in deeper layers as a result of energy straggling. In conventional range-foil ERD, depending on the beam–sample–detector geometry, the best depth resolution can be below the surface because of the large geometrical energy broadening encountered in ERD (Wang *et al.*, 1990). There are several different contributions to depth resolution: resolution of the detection system, energy-loss straggling, multiple scattering, beam energy and angular spread, finite size of the beam spot on the sample, and finite size of the detector. The last three terms together are usually called geometrical straggling and influence the energy resolution because they lead to a spread of possible beam trajectories. The code DEPTH (Szilágyi *et al.*, 1995) uses state-of-the-art theory to calculate the different contributions. Given that very few energy-spread measurements are available, this program is currently the most reliable source for depth resolution. SIMNRA implements the same straggling calculations independently.

Different pitfalls often arise when depth resolution is not well understood. If the energy spread at a given depth is not well calculated (for instance, because of the neglect of multiple scattering or geometrical broadening), then the simulation for sharp interfaces will be sharper than the observed data; the user could then wrongly conclude that the sample has strong interdiffusion between layers or rough interfaces.

Analysts might also be tempted to retrieve more information than the data justify. This is normally done by imposing their favorite model on the data, without testing other possibilities that could also lead to a good fit within the depth resolution at a given depth. In this respect, overreliance on χ^2 goodness of fit, for example, can lead to ultimately incorrect data interpretation, because, as seen in section 15.3.7, the depth resolution used directly affects the results.

15.5 ACCURATE IBA

The ultimate consideration of all analysis is the accuracy available. We use accuracy here in the critical sense, that is, where a measurement can be traced back to international standards of mass, length, and time with a specifiable uncertainty. Because the Rutherford cross section is analytical, the accuracy of RBS is potentially unlimited—except for the major problem in all IBA, the limited knowledge of the energy loss of ions in matter, as discussed in Section 15.4.2. However, there are certain sorts of analysis where the energy loss enters only in second order: one of these cases was treated in detail by Jeynes *et al.* (1997) with the conclusion that, even in this ideal case, several small effects have to be considered (at the 0.25% level) that will cumulatively make an accuracy better than 1% hard to achieve. (We quote all uncertainties here at the 1σ confidence level.)

To our knowledge, the only doubt about the potential accuracy of RBS is the interpretation of the low-energy tails in backscattering spectra. Tails are certainly caused by multiple- and plural-scattering effects and have been calculated successfully with Monte Carlo techniques by Bauer *et al.* (1992, 1993) and by Eckstein and Mayer (1999) for low-energy beams, for which the effects are large. Such tails could also be caused both by slit scattering and any low-energy component that might be present in the beam. However, it has been claimed by Gurbich (1995), on the basis of time-of-flight experiments with a 2 MeV pulsed proton beam and very thin (10 keV) self-supporting gold foils, that the low-energy background cannot be explained by plural, multiple, and slit scattering alone, which would mean that some significant physical phenomenon is still left unaccounted. In any case, the single-scattering approximation certainly fails sometimes: Barradas *et al.* (2007, 2008) pointed out that the calculation of some heavy-ion ERD spectra by the IBA available codes is not consistent with a Monte Carlo calculation; however, it is not yet known

absolutely how reliably these calculation results agree with experiment. Gurbich also does not provide sufficient detail of his Monte Carlo calculation for us to evaluate his result.

In this section, we consider a systematic approach to the estimation of uncertainty, including a discussion of the explicit uncertainty budget that must be included in any standards work that claims to be traceable to international standards. An important benefit of IBA, and the focus of this chapter, is the availability of absolute accuracy, but no analysis has any value unless the analyst is able to reliably specify its uncertainty.

We also include an extended discussion of analytical approaches to the recognition and avoidance of ambiguity in IBA data. It is of great importance for the analyst to recognize the difference between necessary conclusions (required by the data) and valid ones (permitted by the data). In many materials problems to which IBA is applied, the user will want definitive answers from the analyst. The analyst therefore needs to gain skill in seeing objectively what information is really contained in the data and how to apply prior information from the user to eliminate various valid solutions of the data.

15.5.1 Uncertainty estimation

15.5.1.1 Type A and Type B

We start by referring the reader to the *Guide to the Expression of Uncertainty in Measurement* (GUM, 1995). According to GUM, there are two types of uncertainty estimation: Type A and Type B. Uncertainties are of Type A when they can be calculated as a standard error from a set of measurements. They are of Type B when the statistical data needed for Type A calculations are not available and the user has to make a more informal estimate of the probable measurement error. Thus, for example, a measurement of length might be made with a ruler. The experimenter could estimate the uncertainty of a single measurement by assuming a maximum reading error of, say, one-half of a graduation. This would be a Type B estimate. On the other hand, to obtain a Type A estimate the experimenter could make a series of measurements and then determine the average and standard deviation. It is worth noting that Type A estimates are not always better than Type B estimates. In the case of a ruler measurement, for example, there might well be a systematic reading bias from an observer that could go unnoticed. This is not such a trivial point as it seems. Polanyi (1958) rehearses the famous case

> … of the Astronomer Royal, [Nevil] Maskeleyne, who dismissed his assistant [David] Kinnebrook [in 1796] for persistently recording the passage of stars more than half a second later than he, his superior. Maskeleyne did not realize that an equally watchful observer may register systematically different times by the method employed by him; it was only Bessel's realization of this possibility which 20 years later [after considerable work by Bessel, who was the first, in 1838, to observe stellar parallax] resolved the discrepancy and belatedly justified Kinnebrook.

We note further that GUM speaks of "uncertainty" (indicating that our knowledge is limited) rather than "error" (which implies that a mistake has been made). It also uses the idea of "coverage", so that, instead of saying "the 1σ error was 2%", GUM uses the more generalized terminology "the expanded uncertainty was 2% with a coverage factor k = 1". Of course, in all cases, both Type A and Type B uncertainties must be estimated and combined as necessary.

15.5.1.2 Uncertainty budget

The uncertainty budget is specified by GUM as a formal approach to the systematic evaluation of the uncertainty of a measurement, which is essential when a critical result is presented whose traceability must be explicit. This concept was described with special reference to IBA by Wätjen and coworkers (Sjöland *et al.*, 2000). We emphasize again that IBA is a quantitative analytical technique that is capable of great precision and that has well-known uncertainties; we do our users a disservice by not properly estimating these uncertainties.

The uncertainty budget for the analysis of Fig. 15.1 is presented in Table 15.5 as an example. All of the sources of uncertainty are listed, making the origin of the claimed combined standard uncertainty very clear and, hence, easy to evaluate critically. It is clear that the stopping power uncertainty dominates the total combined uncertainty.

Table 15.5. Uncertainty Budget. Coverage factor k = 1. (Reproduced from Jeynes *et al.*, 2006.)

	Type A or B	**IBM detector**	**Cornell detector**	**Comment**
Pileup correction		2.60%	0.80%	
Uncertainty of pileup correction	A	2%	2%	From shape-fitting accuracy
Counting statistics, As signal	A	0.28%	0.47%	
Counting statistics, a-Si signal	A	0.08%	0.13%	
Scattering angle	B	0.28%	0.07%	0.2° and ~1/[$\sin^4(\theta/2)$]
Electronic gain	B	0.5%	0.5%	
Pileup correction	A	0.05%	0.02%	See Section 15.2.4
Relative uncertainty		0.64%	0.70%	
Relative uncertainty of average of two detectors		0.48%		average/$\sqrt{2}$
Beam energy	B	0.20%		Same for both detectors
Rutherford cross section	B	0.16%		Screening correction
Combined standard uncertainty		0.54%		Relative accuracy
IBA code uncertainty	B	0.2%		From software intercomparison (Barradas *et al.*, 2007, 2008) 0.7% for HI RBS; 0.4% for He ERD
Si stopping power	B	0.6%		From software intercomparison (Barradas *et al.*, 2007, 2008) because SRIM-2003 stopping powers were used
Total combined standard uncertainty		0.83%		Absolute accuracy

It is this sort of treatment that is able to establish the traceability of a measurement and, thus, justify the weight put upon it. We note that IBA is very simple, and specifying its traceability to international standards of weights and measures is relatively easy. The present treatment is a significant simplification of the GUM recommendations, which can be applied successfully to much more complicated cases.

15.5.2 Spectral ambiguity

In this section, we follow the treatment of Jeynes *et al.* (2003), which also includes further examples. We show that IBA spectra are grossly ambiguous in general, and we re-analyze the ambiguous spectrum previously discussed masterfully by Butler in 1990 (see Fig. 15.6). There are two approaches to overcoming this ambiguity: the first is to collect multiple spectra under different conditions to constrain the solutions found (where a "solution" is an elemental depth profile that has a spectrum that fits the data), and the second is to rule out, *a priori*, certain types of solution, which

we call “restricting the state space”, where the state space is the multidimensional space containing all possible depth profiles.

We say that an optimal solution is a depth profile from which a spectrum can be calculated that fits the data well and that a spectrum is ambiguous where more than one optimal solutions exist.

For the As implant of Fig. 15.1, for example, one element in the state space is a pure As sample, another is a pure Si sample, and there are a very large number of intermediate elements. The state space is large, but it is not infinite because the energy resolution limits the number of layers that must be considered and the detection sensitivity limits the number of layer compositions that must be considered.

15.5.2.1 Multiple spectra

Every analyst is familiar with the practice of tilting the sample and taking another spectrum to determine which features of the spectrum come from the surface: the surface signal position does not vary with beam incident angle, whereas signals from below the surface will appear to move as the geometry changes. An equivalent way of doing this is to use two detectors at different scattering angles. This is not a new idea: Williams and Möller were using two (or more) detectors in 1978 (although for a rather different purpose; Williams and Möller, 1978), and Edge (1983) reported calculations emphasizing the value of spectra from two detectors but using an iterative method of calculation that is not easy to extend to three or more spectra. Butler (1990) emphasized the value of multiple detectors, and Alkemade *et al.* (1990) demonstrated that, for a sample with n elements, one needs, in principle, to collect n – 1 different spectra to eliminate ambiguity.

Figure 15.1(d) shows an example of the independently collected data from two detectors directly compared. In this case, exactly the same quantity (the depth profile of As) is measured by each detector, and the profiles should overlap. That they do is an indication that the independently determined electronic gain calibrations are reliable. The fwhm values of the As signals are different because the detector energy resolutions are different. The signals at negative depths appear because the channel data are being replotted directly on a depth scale, without correction for broadening due to the detector resolution and straggle.

15.5.2.2 Restricting the state space

It is very easy to demonstrate that RBS spectra are ambiguous. Butler showed an example that is ambiguous in the sense that different depth profiles exist where different partial spectra add up to the same total spectrum; we discuss this interesting case in the next subsection. However, we have not (yet) found any examples where IBA data are systematically ambiguous in the sense that the system is “frustrated” in Kirkpatrick *et al.*’s (1983) terminology, that is, where a number of optimal solutions exist with large potential barriers between them. Other systems that are frustrated are easy to find: see the related discussion of ellipsometry data by Barradas *et al.* (1999b) as an example.

When interpreting such data as the As implants described in Fig. 15.1, analysts are used to tacitly ruling out the possibility of As deep in the sample because they know that, in this case, the substrate is pure silicon. However, Barradas *et al.* (1999a; denoted BJJM) demonstrated that the most probable solution of this type of spectrum, assuming that some oxygen signal is present and that no prior information is available, is that there is a significant quantity of the heavy element in the substrate. This is because any particular spectrum can be reproduced by many mixtures of the three elements, given that the sensitivity to the light element is limited and there is always some uncertainty about the collected charge.

It is important to be objective about what we know about the sample *a priori*. If we assume nothing about the sample, then we have to report a range of possible solutions, consistent with the data. Interestingly, BJJM also demonstrated that, provided that the state space is suitably restricted, RBS data are remarkably unambiguous with respect to collected charge (total number of counts). It is a common pitfall for analysts to collect large amounts of charge to obtain “smooth” data, even though

very small charges (BJJM considered 0.1 μC with a 2.5 msr detector solid angle) can give objectively quite well-determined solutions even for difficult cases, with the right number of layers and qualitatively the right stoichiometry in the layers. Of course, with fewer counts in the spectrum, the statistical uncertainties of the fitted stoichiometry and thicknesses of the layers increase, as expected. It is worth pointing out that this discussion emphasizes the value of backscattering spectra collected simultaneously with microbeam PIXE spectra: Microbeams typically use only 100 pA, and the total collected charge is often a small fraction of a microCoulomb. Do not fall into the related pitfall of neglecting the potentially large amount of information in a noisy spectrum!

15.5.2.3 Butler's example re-analyzed

We show Butler's example of an oxidized NiCrAl alloy in Fig. 15.6. He pointed out that, for this example, the false solutions can be eliminated if prior chemical information is taken into account. Thus, he knows that the oxygen comes from the oxidizing process and, therefore, enters through the surface. (Actually, most of his false solutions can be eliminated simply by excluding O from the substrate.) Moreover, the O binds with the metals in well-known ways. Therefore, the ambiguity is greatly reduced if the analyst can manipulate molecular (rather than atomic) depth profiles.

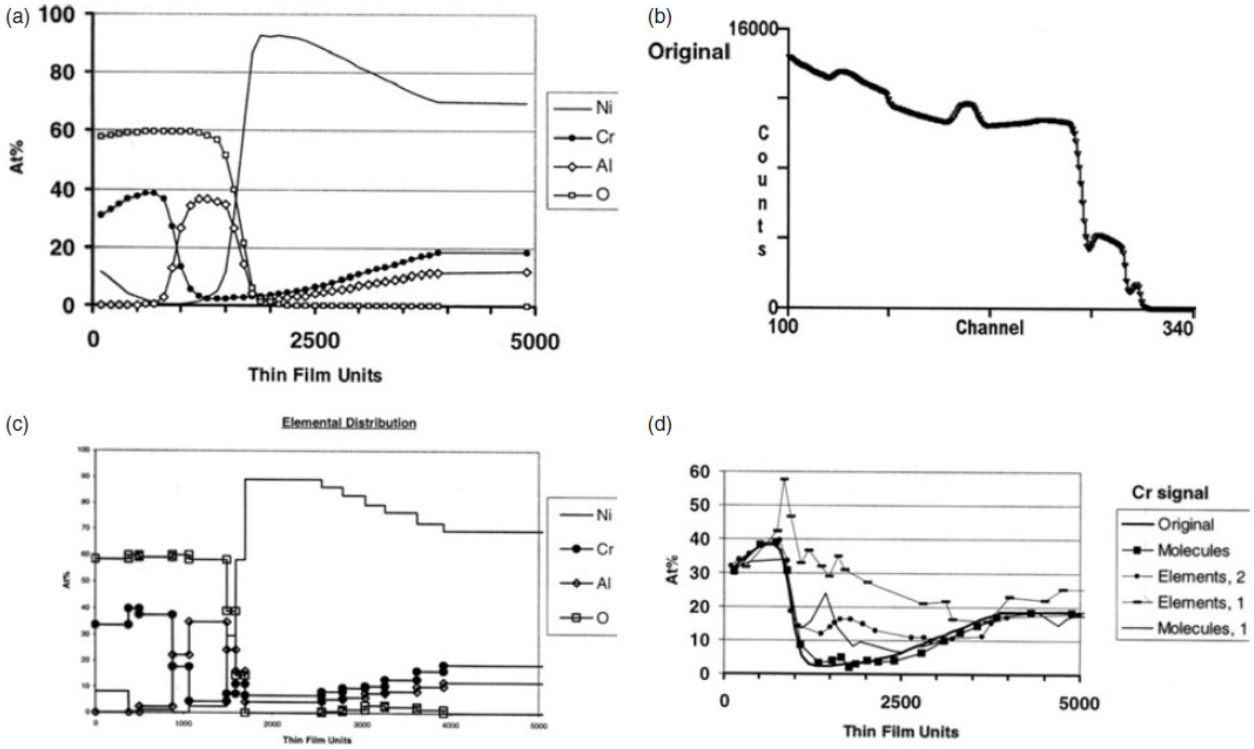

FIG. 15.6. Butler's (1990) example of an oxidized NiCrAl alloy re-analyzed (reproduced from Jeynes *et al.*, 2003). (a) The original profile from which the spectrum was calculated; (b) spectrum (symbols) and fit (line); (c) atomic profile fitted to data assuming molecules and complete oxidation from the surface, using two spectra at different detector angles and excluding alumina from the surface; (d) comparison with the original profile of the Cr profile calculated under various assumptions. Specifying only elements barely constrains the profile, and even with two detectors, the profile is not recovered at intermediate depths. Using only one detector with the assumption of molecules is also not sufficient. The molecules used are NiO, Cr_2O_3, Al_2O_3, and $Ni_{195}Cr_{186}Al_{119}$.

Figure 15.6(a) shows the elemental depth profile of Butler's example, with a spectrum calculated from it shown in Fig. 15.6(b). Figure 15.6(c) shows the solution obtained closest to the original profile, and we discuss this result further below. We point out here that this result is essentially identical to the original, except for some interface broadening (we have not deconvoluted the straggle).

It turns out that the Cr profile is the most sensitive to the prior assumptions of the analysis, and Fig. 15.6(d) shows the Cr profiles obtained under four different assumptions. To retrieve Butler's initial profile unambiguously, one must specify not only the molecules present, but also the following conditions: only oxides are present near the surface, oxygen is excluded from the substrate, Al is excluded from the near-surface region, and two independent spectra were recorded (at different scattering angles in our example). Butler did not point out this last condition for this example, although he noted that, in general, multiple spectra are always a help. These particular data are very ambiguous: many different solutions, all of them as good as that shown in Fig. 15.6(b), can be obtained without any of the conditions mentioned.

In this example, we have allowed the O to exist only when bound to metals, and we have allowed only free Ni to exist. The substrate is specified by a molecule representing the starting alloy composition. It is easy to specify various assumptions about the chemistry to investigate whether they are consistent with the data. If they are not consistent, they can be ruled out. Thus, RBS is an effective tool not just for obtaining a solution to a spectrum, but also for testing a variety of assumptions about the sample against the data.

15.5.3 Model-free analysis and Occam's razor

In the presence of ambiguity, the analyst must be careful to control his assumptions. The philosophical maxim of William of Ockham from the 14th century known as Occam's razor should be kept in mind by all analysts. This maxim is given variously as *Pluralitas non est ponenda sine neccesitate* (plurality should not be posited without necessity) or *Non sunt multiplicanda entia praeter necessitatem* (entities are not to be multiplied except of necessity). Consider how this principle applies to ion beam analysis.

There are many alternative ways to fit any given set of data. If a good fit to the data has been found, it might represent a valid solution. Whether or not it is valid depends on whether correct parameters have been used. Sometimes, this might be an intricate question if one is interpreting the detail of a spectrum. Even if the solution is valid, in the presence of ambiguity, it is not necessarily true. Even if the solution is not false, it might not be useful in the case where Occam's razor has not been wielded. In Butler's example, the spectrum is consistent with a variety of Cr profiles; one can discriminate among these profiles to determine the real one only by restricting the number of parameters describing the system (using Occam's razor), for example, imposing prior chemical assumptions on the system. In this example, four molecules are used instead of four elements, but the light element is correlated with the heavy elements so that, in addition to the number of stoichiometric possibilities being reduced, the insensitivity of the system to the light elements is not allowed to seriously distort the results.

Moreover, analysts sometimes overlook assumptions that they tacitly impose on data when interpreting the data according to a model. For example, the As implant profile of Fig. 15.1 could be fitted with a Gaussian distribution, and many IBA codes facilitate such a fitting. Now, there is nothing wrong with this approach, as long as it is borne in mind that an explicit assumption is being imposed on the data, which can lead to error (that might be large) if the profile is not, in fact, Gaussian. A model-free fit, imposing no prior assumption on the data, would instead involve a number of layers of varying stoichiometry. Occam's razor requires that the number of layers be restricted in order to restrict the number of fitting parameters. Then, there is an explicit tradeoff between the goodness of fit and the number of layers. Clearly, for any given spectrum, the number of fitting layers can be increased uselessly to follow the statistical variation of the spectrum. This underlines the value both of Occam's razor, which highlights and deprecates this uselessness, and of multiple spectra, which have independent statistical variation and thus naturally discourage the use of too many layers.

15.5.4 Common pitfalls in data analysis

Here, we are concerned with some of the problems and issues that are particularly relevant to data analysis. Many prior assumptions are made in all data analysis, some explicitly and other implicitly. All of these assumptions have the potential, if incorrect, to lead to severely wrong results. The assumptions can be divided very roughly into four categories: those related to the sample, the experimental parameters, the physics, and the databases.

Assumptions about the sample include the identities of the elements present; a given depth profile or elemental distribution; and the existence of roughness, inclusions, and other inhomogeneities. The experimental parameters are known with an accuracy that varies widely for different setups. The user might be aware of this accuracy (for instance, a 1 keV beam energy spread) or not (for instance, a 5 keV energy drift with accelerator temperature during an experiment). Assumptions about the physics involved include the interactions both between the analyzing beam and the sample and between the detected particle and the detection system. The user might include only the basic physics given in Section 15.3.3 in situations where some of the phenomena described in Section 15.3.4 play a vital role. Using a given stopping or scattering cross section is an implicit assumption that the data base used are correct for that case. Moreover, the prior assumptions are often related to each other. For instance, an assumption about the scattering angle implies a consistent assumption about the scattering cross section.

We list in Table 15.6 the consequences for data analysis of some of the problems that commonly arise as a result of incorrect assumptions, along with steps that can be taken to prevent or remedy such problems. These preventive and corrective actions can be divided into four main groups: First and foremost, knowledge about the setup used and its characteristics should be as complete and accurate as possible. This often involves elaborate experiments or even the installation of new hardware (for instance, to measure the beam charge) and is generally not feasible in the short run. Second, alternative experiments, using different beams, energies, and other parameters or even completely different techniques, might be required. Additional beam time or other techniques, however, are not always available. Third, programs that include the best physical models and databases available for the problem at hand should be used. This is often the only practical alternative for the data analyst, who is thus often confronted with problematic data.

Table 15.6. Pitfalls and remedies in data analysis.

Assumption about	What went wrong	Possible consequences	What can be done*
Elements present	Impurities ignored	Impurity signal wrongly assigned to some other element (possibly one with a small cross section, leading to large effects on the overall solution)	Use a complementary technique that can detect the impurities; link the impurity to a major element.
	"Missing element" falsely postulated or ignored	Wrong fitted charge to accommodate the unobserved element, with consequences for all other elements	Use a complementary technique that can detect the missing element; collect spectra under different experimental conditions.
Depth profile	False depth profile chosen, leading nevertheless to a good fit (IBA is often ambiguous)	Completely wrong results	Collect spectra under different experimental conditions; test different models.
	Profile function (such as Gaussian) imposed on some element when real profile is different	Inaccurate results for that element; if signal is superimposed on other fast-changing signals, other elements possibly affected as well	Perform a model-free analysis; test different models.
	Sample roughness ignored (often the case in interdiffusion studies)	Obtained depth profile too broad or completely wrong in severe cases	Measure roughness; perform grazing-angle experiments.
	Wrong type of sample roughness considered	Derived roughness parameters meaningless	Determine roughness type; include it in analysis if possible; test different models.
Beam energy	Calibration of accelerator inaccurate	Systematic error in analysis (can be partially compensated for RBS by MCA calibration and stopping); EBS cross sections wrong; depth scales wrong	Calibrate the accelerator energy!
	Energy drifted during the experiment	Apparent energy resolution worse than expected; apparent gain changes; slight changes in cross sections, leading to inaccuracy in the quantification	Measure energy drift by collecting calibration spectra at the beginning and end of each run; discard badly affected data.
Scattering angle	Poor original measurement; problem with moving detector	Completely wrong results; near-normal incidence and grazing-angle experiments inconsistent	Determine accurately (might be difficult); treat as a fit parameter.
Angle of incidence	Poor alignment of sample holder; problem with goniometer	Completely wrong results; near-normal incidence and grazing-angle experiments inconsistent	Align sample holder (might be difficult); treat as a fit parameter.
Energy resolution	Not determined recently	Small error in results; can be crucial if interdiffusion or roughness are important	Determine energy resolution in each run; treat as a fit parameter.
Solid angle	Not well determined; might change with sample distance	Normally assigned to collected charge, leading to an extra error in the results	Determine accurately (might be difficult); adjust for sample distance.
Beam charge	Not well determined (or not measured)	Not very important if the spectrum includes some signal (normally substrate) that can serve as internal calibration; completely wrong results otherwise	Determine accurately (might be difficult or impossible); rely on internal normalization (might be difficult or impossible); treat as a fit parameter.

Stopping power	Database inaccurate	Inaccurate elemental concentrations and layer thicknesses; completely wrong analysis in severe cases	Use a better database if available; determine the relevant stopping powers if possible; perform experiment with a different beam; treat as a fit parameter.
	Bragg rule for molecular stopping inaccurate	Inaccurate elemental concentrations and layer thicknesses; completely wrong analysis in severe cases	Use molecular stopping powers if available; determine them if possible; performing an experiment with a different beam is unlikely to help.
Scattering cross section	Required non-Rutherford (EBS or NRA) cross section might not be measured or determined yet or might be inaccurate	Inaccurate elemental concentrations; completely wrong analysis in severe cases	Determine the relevant cross section; exclude the element involved from the analysis; perform experiment with a different beam/energy.
	Calculated cross section for an EBS (or NRA) resonance at a given depth for the average beam energy at that depth	Inaccurate elemental concentration and depth profile of affected element; completely wrong analysis in severe cases	Use codes that correctly integrate cross section over the entire energy distribution of the analyzing beam before scattering.
Straggling	Used Bohr straggling where Bohr model is not valid	Incorrect diffusion, mixing, and roughness results	Always use the best models available.
	Did not include Tschalär effect	Incorrect diffusion, mixing, and roughness results for depths where energy loss is 10–20% larger than initial beam energy	Always use the best models available.
Plural scattering	Ignored when relevant	(Heavy) Elements introduced at depths where they do not exist	Use the best models available whenever plural scattering is relevant.
Multiple scattering	Ignored when relevant	Incorrect diffusion, mixing, and roughness results	Use the best models available whenever multiple scattering is relevant.
	Not well calculated, particularly at grazing angles	Incorrect results	Monte Carlo techniques might be the only available alternative; perform experiment with a different beam.
Channeling	Unnoticed accidental channeling overlooked in analysis	Incorrect results; but if only the substrate signal is affected, there might be no consequences unless the substrate signal is used for normalization	Adjust incidence angle; rotate sample while measuring; calculate channeling.
Pulse pileup	Ignored when relevant	(Heavy) Elements introduced at depths where they do not exist; signal heights and areas affected; dramatically degraded accuracy	Accurate models exist—use them!
Poorly fitted data	Could not find correct model	Completely wrong results	Reliable analysis requires well-fitted data.

Acronyms: EBS, elastic backscattering spectrometry; MCA, multichannel analyzer; NRA, nuclear reaction analysis; RBS, Rutherford backscattering spectrometry.

*Caution should be used where the suggestion is to treat a variable as a fit parameter, as this could lead to even larger errors!

This leads to the fourth and most important group of preventive actions, which is to avoid both overinterpretation and underinterpretation of the data. Overinterpretation occurs whenever the data analyst unjustifiably imposes a given model on the data. This often leads to tuning the experimental parameters beyond their known accuracy (such as increasing the charge while scaling the stopping power for a given element in a given layer). The user must consider different models that might lead to an equivalent or better solution. Of course, the prior assumptions that the analyst can impose on data to exclude certain valid solutions, discussed in Sections 15.5.2 and 15.5.3, are also strictly overinterpretations, but in this case, they are explicitly justified.

Underinterpretation occurs when the analyst does not extract all of the information that is actually present in the data. For instance, signal widths, which are often disregarded, can provide information on both intermixing and roughness. The analyst might not be interested in that further information, but often, it is simply due to lack of knowledge (for instance, that new-generation codes can extract roughness information with considerable ease). However, most often, underinterpretation occurs when the data are not well fitted. Modern codes are now available that facilitate excellent fitting of spectra, enabling the analyst to put much greater weight on the results.

As a general rule, it is always desirable to collect multiple spectra from the same sample. This can be done using multiple detectors installed in the experimental chamber or by performing different experiments including different techniques. Although this is not necessary in simple cases, to analyze complex samples meaningfully, multiple spectra and multiple techniques are almost always required. The typical example is to use RBS, EBS, ERDA, and PIXE to be sensitive to the heavy elements, specific light elements, hydrogen, and minor contaminants. All spectra collected should be analyzed simultaneously with the same depth profile, to ensure a self-consistent analysis.

A major pitfall is the use of the wrong value for the product of the charge and solid angle, $Q\Omega$, where normalization of this quantity is not easily available from the spectrum. $Q\Omega$ is implicitly determined by the composition of the sample (where there is no channeling), so that, if the wrong value is imposed on the data, the results can be severely distorted. An illuminating example in which the uniqueness of $Q\Omega$ was used to determine the sample composition with great elegance was reported by Lee *et al.* (2006)

Finally, an outstanding pitfall to be avoided is the overinterpretation of poorly fitted data, which must always be treated with great caution. Given that particle scattering spectra are not easily inverted into depth profiles, because the signal at a particular channel can come from various elements at different depths, if the spectrum is poorly fitted, the model could be entirely wrong! In particular, the fact that part of the spectrum can be fitted perfectly does not mean that the model is partly correct. A particle scattering spectrum is an object with some "holographic" properties: its parts are interdependent. Of course, no spectrum is perfectly fitted, but the analyst should ensure both that the fit is qualitatively correct for the entire spectrum and that misfitting regions are understood properly. For example, the low-energy signal is not usually well fitted because multiple-, plural-, and slit-scattering effects are generally neglected.

Two main conclusions can be made: Reliable analysis requires well-fitted data. However, a well-fitted spectrum implies only the validity of the model, not its truth.

15.6 UNWANTED TARGET–BEAM INTERACTIONS

15.6.1 Beam-induced heating

The power deposited in a target under beam impact can be expressed in watts through the product of the particle energy (in megaelectronvolts) and the number of particles per second (in microamperes), where the latter represents particle current, not electrical current. If the cross-

sectional area of the beam is known, then the power density (watts per unit area) is also readily calculated. Basic heat-flow calculations can then be made.

For a target of semi-infinite thickness, the validity of this calculation rests on the fact that the fraction of incident particles reflected or scattered out of the target is negligible (<1%), which is true for all beams at megaelectronvolt energies. It further requires that secondary particle emission (sputtered particle flux, nuclear reaction product flux, electron emission, etc.) produces no secondary heating effects. Again, for megaelectronvolt particles, this assumption is usually satisfied. For thin targets, the heat input is determined by the energy deposited by the beam within the target, which might be much less than the incident energy. Although it is usually of no interest in ion beam analysis applications, heat generation in the target proceeds through the same fundamental interactions that have been identified in discussions of "spike" phenomena. Beam energy expended through electronic stopping is coupled to electrons, that is, the electrons are "heated", and this excitation must then be coupled to the lattice through electron–phonon interactions, thereby producing macroscopic sample heating with a characteristic time constant of picoseconds. The route to lattice heating is more direct in the nuclear stopping regime, which dominates near the end of the particle range. As noted above, however, the quantity of interest is usually the mean power deposited. The variation in rate of thermalization of the lattice with depth is rarely of concern.

The sample response to beam heating depends on experimental conditions. If the beam spot is small in area, radial symmetry can be assumed. At temperatures above a few hundred degrees Celsius, cooling is dominated by the radiative mechanism (T^4), rather than by conduction. (When conductivity within the sample is good, temperature profiles are rather unremarkable.)

However, mechanical contact does not ensure good thermal contact, and thermal contacts are notoriously hard to make in a vacuum. The existence of a hot spot can lead to

- differences in electron emission;
- differences in sticking probabilities for adsorbates (e.g., O_2. CO, H_2O) and, thus, lower coverages relative to cooler surrounding material;
- varying decomposition rates for adsorbed hydrocarbons; and
- annealing of beam-induced disorder.

Thermal gradients can result in the redistribution of mobile impurities, including embedded gas atoms from the beam, and can cause decomposition of materials. The question of how best to determine the target temperature under the beam lies beyond the scope of these comments. Schultz *et al.* (1992) showed how important temperature control can be: they reported large changes (up to an order of magnitude) in the level of residual disorder in megaelectronvolt energy self-irradiation of Si over the temperature range of 270–320 K for otherwise identical irradiation conditions. Hence, significant changes in beam-induced disorder can result from beam heating of even a few degrees.

It is worth emphasizing that beam-induced heating effects are exacerbated when a microbeam is used because the beam current density is significantly increased during the mirobeam analysis.

15.6.2 Beam-induced radiation damage

In many IBA applications, radiation damage produced by the ion beam is a key limitation. In general, such effects depend not only on the primary energy-loss process involved, but also on subsequent solid-state diffusion effects. Hence, the nature and temperature of the target, the dose rate, and the total fluence are all relevant parameters. The review literature on radiation damage is extensive (see, for example, Grubb, 1974; Weber *et al.*, 1997; Averback and de la Rubia, 1998), and we provide here only some simple guidelines to assist newcomers in the IBA field.

Radiation damage processes arise from two widely different mechanisms of energy transfer:

- In nuclear (or atomic) stopping, $(dE/dx)_n$, scattering of the incident ion by the (partially) screened target nucleus results in significant momentum being transferred to the whole atom. This contribution is the dominant energy-loss process at low (kiloelectronvolt) energies, but at energies common in IBA (~1 MeV/nucleon), it is only a very small fraction (~0.1%) of the total stopping process.
- In electronic stopping, $(dE/dx)_e$, energy is lost to various electronic excitation and ionization processes.

In metals and most semiconductors, electronic excitation and ionization both decay almost instantaneously without producing permanent damage effects. In such materials, the major source of radiation damage is the small nuclear stopping component (first mechanism, above). An upper limit to the resulting defect density can be obtained by multiplying the nuclear stopping power, $(dE/dx)_n$ (in eV 10^{-15} cm^2), by the total ion fluence and dividing by twice the displacement energy, E_d. At IBA energies, the nuclear stopping power is usually between 0.03 eV 10^{-15} cm^2 and 0.3 eV 10^{-15} cm^2, and E_d is typically ~30 eV. Hence, a beam fluence of 10^{15} ions/cm^2 produces, at most, a defect density in the 0.05–0.5% range.

On the other hand, in insulators and other molecular compounds, damage production rates are often considerably greater because, in this case, the electronic stopping power (second mechanism, above) can also cause bond breakage and, hence, permanent chemical and structural changes in the target. Radiation chemistry studies in a wide variety of inorganic and organic molecular solids, using electron, γ-ray, and megaelectronvolt ion bombardment, have shown that the number of bonds broken per 100 eV of deposited energy (the so-called g factor) is roughly 10, indicating that, in such materials, electronic stopping processes are usually more effective in breaking bonds than the nuclear collision cascades. For example, Benyagoub (2006) showed that the fraction, g, of electronic energy loss converted to heat is 0.124 for zirconia and 0.129 for hafnia. Because the electronic stopping power at IBA energies is two to three orders of magnitude greater than the nuclear stopping power, it is evident that the total rate of damage creation in insulators can be as much as 10^3 times greater than the nuclear collision estimates in the previous paragraph.

In practice, the observed levels of damage vary widely from one type of insulator to another. We have presented here only a rough estimate of the maximum rate at which damage is created; in many materials, self-annealing reduces the damage. For example, most ceramic materials (WC, BN) and certain inorganic oxides (MgO, $A1_2O_3$, SiO_2, UO_2) are fairly resistant, whereas alkali halides, polymers, and most organic and biological materials are rapidly and permanently decomposed by electronic stopping processes. In particular, the beam is actually capable of rapidly drilling holes in poly(tetrafluoroethylene) (PTFE) (Grime *et al.*, 2005).

Damage creation due to electronic stopping is not restricted to insulators; rather, it can occur in any polyatomic molecular solid, including high-T_c superconductors.

Finally, it should be emphasized that, even when a large amount of damage is created by the analyzing beam, this does not necessarily introduce significant error into the quantities being analyzed. However, if some of the resulting defect species are mobile (radiation-enhanced diffusion) or volatile (for example, H_2), then significant changes in depth distribution or stoichiometry might result. In some cases, low-temperature analysis can reduce the problem.

Single-crystal targets, which involve RBS/channeling analyses, are particularly sensitive to all types of radiation damage, even when the resulting defect species are immobile. Interactions between solute atoms and point defects (vacancies or interstitials), for example, can cause solute atoms to move into a completely different lattice site configuration (see Chapter 12, Section 12.5.5).

Again, it is worth emphasizing that beam-induced damage effects are exacerbated when a microbeam is used.

15.6.3 Beam-induced sputtering

As part of the radiation damage process, near-surface atoms occasionally receive sufficient kinetic energy or electronic excitation to be ejected—sputtered—from the target surface. Obviously, if the amount sputtered during IBA becomes significant (10^{15} cm^{-2} ≈ one monolayer), then the such properties as the surface structure, stoichiometry, and film thickness could be irreversibly changed. Again, as in the radiation damage section, we divide the discussion into two widely different types of behavior.

In metals and most semiconductors, only the nuclear stopping component contributes to sputtering, and the observed yield is directly proportional to $(dE/dx)_n$ evaluated at the target surface, that is, at the incident beam energy, E_0. The relationship between the sputtering yield, Y (atoms/incident ion), and $(dE/dx)_n$ [eV/(10^{15} atoms cm^{-2})] can be expressed as

$$Y = \frac{0.1(dE/dx)_n}{U_s \cos\phi}. \tag{15.4}$$

The numerator $[0.1(dE/dx)_n]$ is a rough estimate of the total energy (in eV) contributing to the sputtering process, U_s (the surface binding energy of the target) is usually between 2 eV/atom and 10 eV/atom, and ϕ is the angle between the incident beam direction and the surface normal. Andersen (1987) showed, fortuitously, an exceptionally good theoretical description of the sputtering behavior of Ni (a typical metal) as a function of the energy and atomic number of the incident beam. The maximum sputtering yield is about 10^{-2} Ni atoms/incident ion for about 1 keV H and about 8 Ni atoms/ion for 100 keV Xe. In general however, the agreement between predicted and measured sputtering yields is no better than a factor of 2.

In the low-energy regime (10–100 keV), where $(dE/dx)_n$ reaches its maximum value, sputtering yields as large as 10 atoms/ion are often encountered. However, at IBA energies, $(dE/dx)_n$ is in the range of 0.03–0.3 eV/(10^{15} atoms cm^{-2}); hence, the sputtering yield is less than 10^{-2}.

In insulators, the collision cascade mechanism of sputtering (described above) still occurs, and hence, sputtering yields of at least 10^{-3} atoms/ion occur in all IBA studies. In insulators, however, the much larger $(dE/dx)_e$ process can also produce significant sputtering through a variety of mechanisms: for example, bond breaking, "Coulomb explosion" effects, and formation of volatile products (H_2, O_2, etc.). The exact mechanisms are, in general, not well characterized, and they depend markedly on the type of insulating material involved. Nevertheless, experimental evidence (Tombrello, 1984) shows that the sputtering yield in insulators can be as high as 10 atoms/incident ion (in rare cases, even 100 atoms/incident ion). In such materials, the electronic stopping process has enhanced the sputtering rate by as much as 10^4.

Note that, in polyatomic targets, preferential sputtering of certain atomic species can often occur. Hence, whenever the total amount sputtered is greater than one monolayer (~10^{15} cm^{-2}), significant changes in near-surface stoichiometry can also result. An extreme example is the rapid dehydrogenation (or graphitization) of polymers that occurs during IBA with megaelectronvolt He^+ beams [see, for example, the review of polymer damage by Brown (1986)].

15.6.4 Charging in insulators

Compared to metals and semiconductors, most insulating materials present a series of special problems with respect to IBA. In the preceding section on beam-induced damage, the greatly enhanced sensitivity of insulators to beam-induced effects such as radiation damage and sputtering was already emphasized. Here, we briefly note two additional complications that arise in certain types of insulating materials: target charging and photon emission.

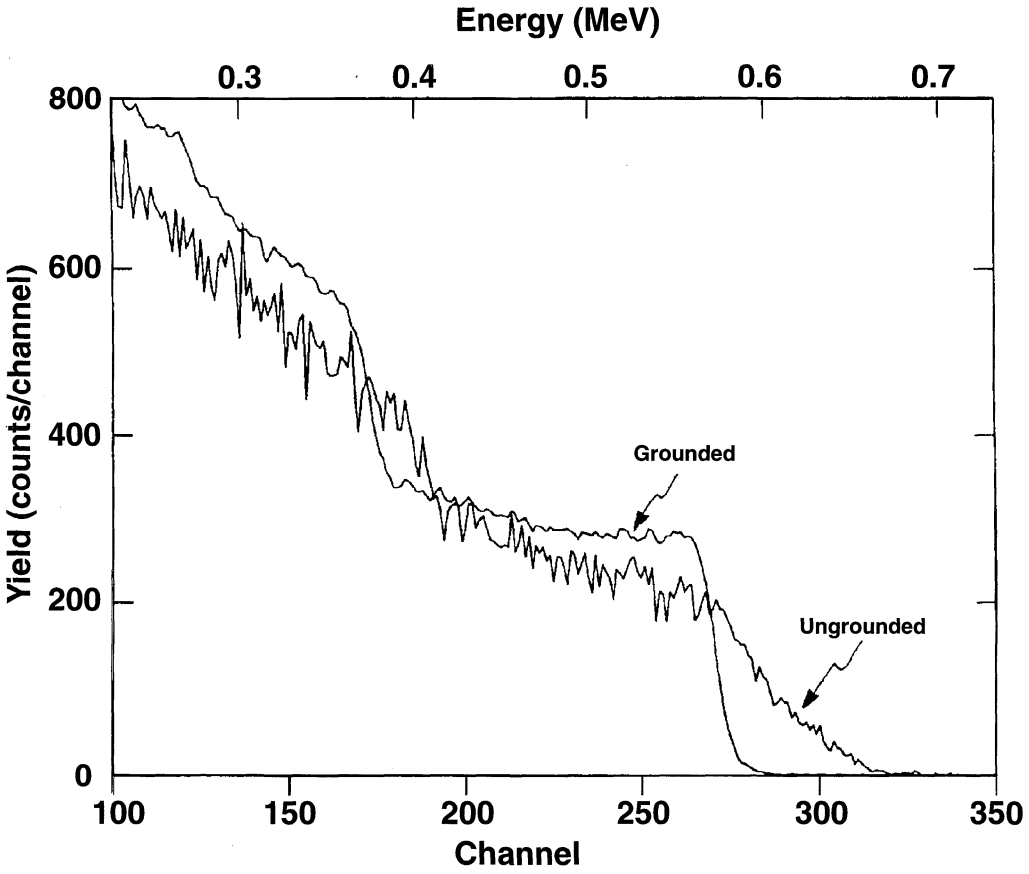

FIG. 15.7. Surface charging effect. Comparison of RBS spectra from a quartz target using 1 MeV ^{4}He: ungrounded and grounded through a thin conductive surface layer of graphite by rubbing a pencil lightly across the surface (Almeida and Macauley-Newcombe, private communication 1991).

Depending on the geometry, thickness, and resistivity of the target material, surface charging under megaelectronvolt ion bombardment can, in severe cases, reach several tens of kiloelectronvolts (Kim *et al.*, 2003). (This value is, of course, still small compared to the incident beam energy, unlike the insulator situation encountered in Auger and secondary ion mass spectroscopy.) However, because the charge states of the incident and backscattered beam are not necessarily the same, surface charging can seriously distort the energy and, hence, the shape of the observed RBS spectrum, as shown for the case of quartz in Fig. 15.7. Because the backscattered He particles are mainly $^4He^{2+}$, one can use $^4He^{2+}$ as the incident beam to reduce the charging-induced energy shift in the RBS analysis of insulating specimens.

Furthermore, surface charging sometimes produces sufficiently high electric fields to interfere with the performance of the Faraday cup system. Also, in certain insulators (for example, $BaTiO_3$), excessive surface charging can even cause the target to disintegrate.

One effective way to neutralize surface charging effects is to provide a supply of low-E electrons from a small, hot filament located nearby. If such a filament is powered through an isolation transformer and is electrically connected to the target holder through a suitable (+50 V) bias to prevent electrons from escaping to the chamber walls, then quantitative current integration can still be achieved. Generally, the use of a transmission Faraday cup is a better way to solve these current integration problems.

Other possible methods that have been used to reduce surface charging include

- coating the surface at least partially with a very thin layer of conducting material, such as graphite (for example, rubbing a pencil lightly across the surface sometimes works) or an evaporated metal (or carbon), and

- sweeping the beam so that it also bombards the adjacent (metal) target holder or a suitably placed metal grid in front of the target, which generates a supply of secondary electrons to neutralize the positively charged surface of the insulator.

In many insulators, charging effects are small enough to be ignored, or discharge by surface tracking can be encouraged by performing the analysisclose to a contact.

15.6.5 Photon emission in insulators

In insulators, much of the electronic excitation resulting from the $(dE/dx)_e$ stopping mechanism is eventually converted into optical emission in the visible and ultraviolet regions. Polymers, alkali halides, and other materials are transparent to such radiation. Consequently, photons emitted even from a depth of several microns can readily escape from the target. In such cases, hundreds or even thousands of photons can be emitted per incident ion. We have already discussed how these photons can generate a flux of secondary electrons at the chamber walls. Furthermore, the energy resolution of charged-particle detectors can be seriously degraded by photogeneration of carriers in the depleted region. (The standard surface barrier detector has a Au electrode with a thickness of ~20 nm that is transparent to visible light.)

15.7 OTHER EFFECTS

15.7.1 Surface and interface roughness

In experiments where the incident or emergent charged particle makes a small angle (for example, <15°) with a target surface that is not smooth, problems in the shape of the energy distribution can arise as a result of the surface topography. This is very often the case for ERDA measurements (see Chapter 5). Even at near-perpendicular incidence, materials such as porous targets and sintered powders can introduce very serious surface roughness complications, leading to data that are either impossible or troublesome to analyze or that do not carry useful information. Recently, Molodtsov *et al.* (2008) reported a method for handling spectra from very rough samples, but this algorithm is not yet implemented in IBA codes.

When roughness is moderate (that is, when it is not so great that it destroys spectral features), IBA can be used effectively to study surface and interfacial roughness. Different methods have been developed. The simplest one is to average spectra calculated for different sample structures, for example, if the roughness leads to a layer with changing thickness. Full Monte Carlo simulations have also been performed. A fast and often efficient approach is to calculate the broadening of observed features due to specific types of roughness. Calculations of the effect of voids, inclusions, and quantum dots are also included in some codes (Barradas, 2001; Mayer *et al.*, 2005).

However, it is normally impossible to determine, from IBA techniques alone, whether the broadening of a given peak or edge is due to roughness, interdiffusion, or an unexpected depth profile of the affected element. Interpretation of the data almost always requires extra information about the sample at hand from some other source. Different microscopies are often employed for that purpose.

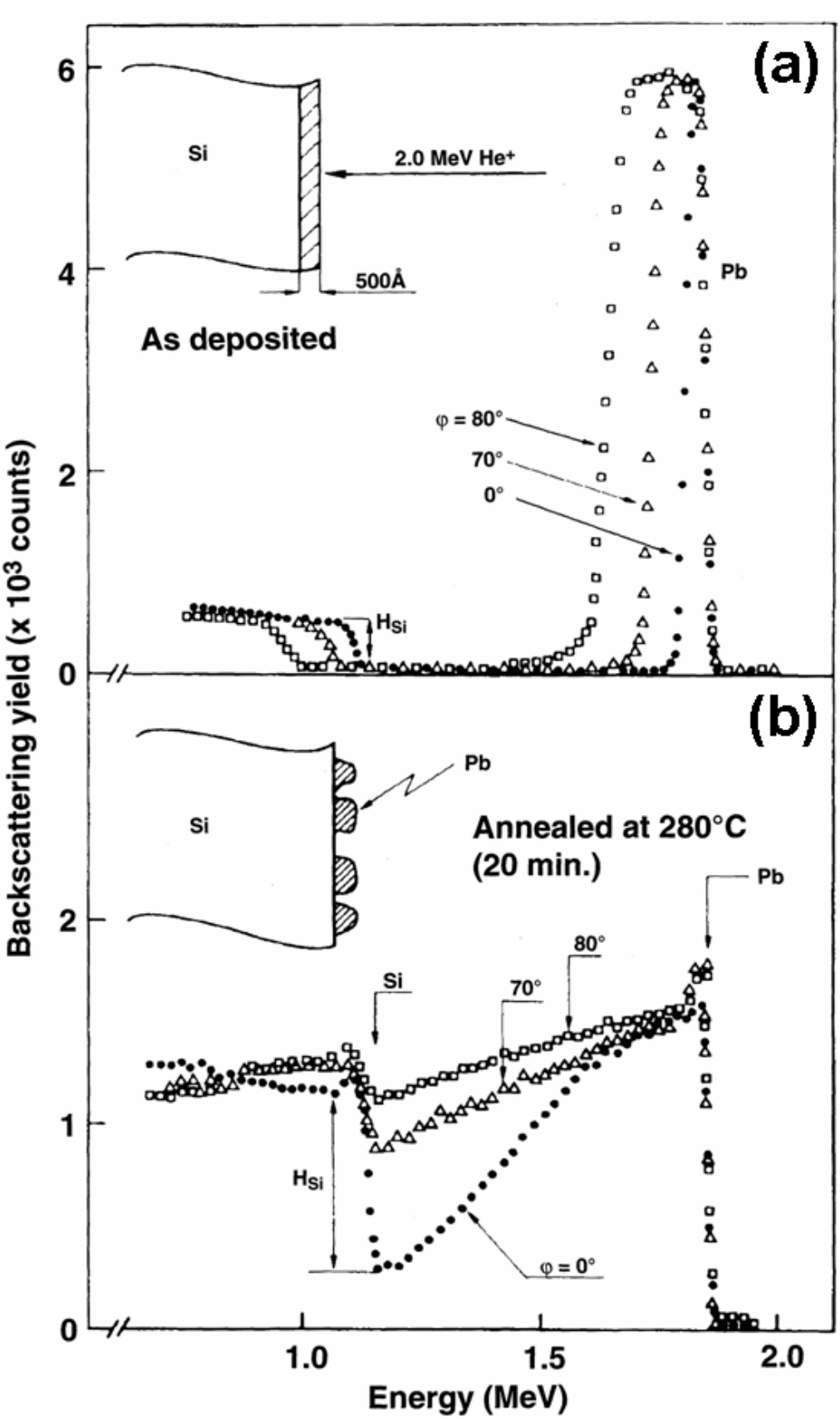

FIG. 15.8. Ambiguity in RBS between roughness and diffusion. Backscattered energy spectra for several tilting angles: (a) from a uniform Pb layer (50 nm) on a Si substrate and (b) from the same layer after being annealed for 20 min. at 280°C (Campisano *et al.*, 1978).

15.7.2 Target nonuniformity

Care must be taken in basing the interpretation of RBS spectra on limited data. Apparently simple features can be misleading if it is assumed that the target has lateral uniformity under the analyzing beam. As shown by Campisano *et al.* (1975), the shape of a Pb spectrum recorded from a nonuniform surface film of Pb on Si can closely resemble that of a laterally uniform diffusion profile of Pb in Si.

This confusion is removed by supplementary measurements and analysis (Campisano *et al.*, 1978). As shown in Fig. 15.8(a), the consequences of varying the target angle, ϕ, with respect to the incident beam for a Pb film of 50-nm thickness overlaying a Si substrate are to give a familiar $(\cos \phi)^{-1}$ broadening of the Pb profile in the RBS spectrum and a correlated shift in the leading edge of the Si continuum. Completely different profiles are obtained for samples that have been annealed to 280°C for 20 min., after deposition. In this case [Fig. 15.8(b)], the decrease in the scattered particle yield, H_{Si}, from Si atoms at the surface as the tilting angle (ϕ) increases rules out interdiffusion. The results were modeled in terms of raised Pb features (islands), and good agreement was found with island dimensions and spacings measured by scanning electron microscopy (SEM) analysis, which displayed the altered surface morphology. RBS methods have been used very effectively by Zinke-Allmang and co-workers (Carlow *et al.*, 1997) to study the development of layer-by-layer and island growth (Stranski–Krastanov films).

15.7.3 Thin film units

Thin film units (10^{15} atoms/cm^2) are the natural units for IBA because the energy loss is measured in eV/(atoms/cm^2), and one monolayer is on the order of 10^{15} atoms/cm^2.

Energy loss is measured in these units because an accurate measure of thin-film thickness is in terms of μg/cm^2 (equivalent to atoms/cm^2 if the stoichiometry is known) and the most reliable way to measure the thickness of a thin film is to weigh it and measure its area. Linear thicknesses (in nanometerss) are unreliable because the densities of thin films can be markedly different from the bulk values and because surface contamination (including oxides) and other surface effects can be large for thin films.

IBA is an ideal technique for measuring thin-film profiles where the composition changes with depth. In these cases, the appropriate density to use depends on the chemistry of the sample, and assuming different chemistries will lead one to infer a different density profile. Therefore, the most neutral representation of IBA-measured depths is in terms of μg/cm^2; thin film units are very convenient and do not involve the sample density, but do assume that the stoichiometry is known.

The pitfall that must be avoided is forgetting that presenting depth profiles with a linear depth scale (in nanometers) hides assumptions about the density of the sample, which might not be well known and might be greatly different from what is expected. Some IBA codes allow the analyst to fit the data using molecules and mixtures of molecular densities. In Fig. 15.6, for example, the depth scale is in thin film units. To plot the profiles in nanometers, one must correctly assign the oxide densities, which is not an entirely trivial exercise.

Acknowledgement

This work is a revision of, and incorporates part of the previous 1992 IBA Handbook (the “Black Bible”) Chapter 12 by J.A. Davies, W.N. Lennard, and I.V. Mitchell. The section on electronic noise is by Max Döbeli (Zurich).

References

Abel, F., Amsel, G., d'Artemare, E., Ortega, C., Siejka, J., and Vizkelethy, G. (1990), *Nucl. Instrum. Methods* **B45**, 100.

Alexander, T.K., Ball, G.C., Lennard, W.N., Geissel, H., and Mak, H.-B. (1984), *Nucl. Phys.* **A427**, 526.

Alkemade, P.F.A., Habraken, F.H.P.M., and van der Weg, W.F. (1990), *Nucl. Instrum. Methods* **B45**, 139.

Allison, S.K. (1958), *Rev. Mod. Phys.* **30** (4), 1137.

Amsel, G., and Samuel, D. (1967), *Anal. Chem.* **39**, 1689.

Amsel, G., and Davies, A. (1983), *Nucl. Instrum. Methods* **218**, 177.

Amsel, G., Girard, E., Vizkelethy, G., Battistig, G., Girard, Y., and Szilágyi, E. (1992), *Nucl. Instrum. Methods* **B64**, 811.

Andersen, H.H., Besenbacher, F., Loftager, P., and Möller, W. (1980), *Phys. Rev.* **A21**, 1891.

Andersen, H.H. (1987), *Nucl. Instrum. Methods* **B18**, 321.

Arstila, K., Sajavaara, T., and Keinonen, J. (2001), *Nucl. Instrum. Methods* **B174**, 163.

Audi, G., Wapstrab, A.H., and Thibaulta, C. (2003), *Nucl. Phys.* **A729**, 337.

Averback, R.S., and de la Rubia, T.D. (1998), *Solid State Phys.* **51**, 281.

BAM (2009), BAM-S107, BAM-S108, BAM-S109, and BAM-S110, in *Catalogue of Certified Reference Materials*, Bundesanstalt für Materialforschung und -prüfung (BAM), Berlin, Germany.

Banks, J.C., Browning, J.F., Wampler, W.R., Doyle, B.L., LaDuca, C.A., Tesmer, J.R., Wetteland, C.J., and Wang, Y.Q. (2004), *Nucl. Instrum. Methods* **B219-220**, 444.

Barradas, N.P., Jeynes, C., Jenkin, M., and Marriott, P.K. (1999a), *Thin Solid Films* **343–344**, 31.

Barradas, N.P., Keddie, J.L., and Sackin, R. (1999b) *Phys. Rev.* **E59** (5), 6138.

Barradas, N.P. (2001), *J. Phys. D: Appl. Phys.* **34**, 2109.

Barradas, N.P. (2002), *Nucl. Instrum. Methods* **B190**, 247.

Barradas, N.P., Jeynes, C., Webb, R.P., and Wendler, E. (2002), *Nucl. Instrum. Methods* **B194**, 15.

Barradas, N.P. (2004), *Nucl. Instrum. Methods* **B225**, 318.

Barradas, N.P., and Reis, M.A. (2006), *X-ray Spectrom.* **35** (4), 232.

Barradas, N.P., Arstila, K., Battistig, G., Bianconi, M., Dytlewski, N., Jeynes, C., Kótai, E., Lulli, G., Mayer, M., Rauhala, E., Szilágyi, E., and Thompson, M. (2007), *Nucl. Instrum. Methods* **B262**, 281.

Barradas, N.P., Arstila, K., Battistig, G., Bianconi, M., Dytlewski, N., Jeynes, C., Kótai, E., Lulli, G., Mayer, M., Rauhala, E., Szilágyi, E., and Thompson, M. (2008), *Nucl. Instrum. Methods* **B266**, 1338.

Barradas, N.P., and Jeynes, C. (2008), *Nucl. Instrum. Methods* **B266**, 1875.

Bauer, P., and Bortels, G. (1990), *Nucl. Instrum. Methods* **A299**, 205.

Bauer, P., Steinbauer. E., and Biersack, J.P. (1992), *Nucl. Instrum. Methods* **B64**, 711.

Bauer, P., Steinbauer, E., and Biersack, J.P. (1993), *Nucl. Instrum. Methods* **B79**, 443.

Benyagoub, A. (2006), *Nucl. Instrum. Methods* **B245**, 225.

Bianconi, M., Abel, A., Banks, J.C., Climent Font, A., Cohen, C., Doyle, B.L., Lotti, R., Lulli, G., Nipoti, R., Vickridge, I., Walsh, D., and Wendler, E. (2000), *Nucl. Instrum. Methods* **B161–163**, 293.

Blaauw, M., Campbell, J.L., Fazinić, S., Jakšić, M., Orlic, I., and Van Espen, P. (2002), *Nucl. Instrum. Methods* **B189**, 113.

Brice, D.K., and Doyle, B.L. (1990), *Nucl. Instrum. Methods* **B45**, 265.

Brown, W.L. (1986), *Radiat. Eff.* **98**, 115.

Butler, J.W. (1990), *Nucl. Instrum. Methods* **B45**, 160.

Boudreault, G., Claudio, G., Jeynes, C., Low, R., and Sealy, B.J. (2004a), *Nucl. Instrum. Methods* **B217** (1), 177.

Boudreault, G., Elliman, R.G., Grötzschel, R., Gujrathi, S.C., Jeynes, C., Lennard, W.N., Rauhala, E., Sajavaara, T., Timmers, H., Wang, Y.Q., and Weijers, T.D.M. (2004b), *Nucl. Instrum. Methods* **B222**, 547.

Campisano, S.U., Foti, G., Grasso, F., and Rimini, E. (1975), *Thin Solid Films* **25**, 431.

Campisano, S.U., Ciavola, G., Costanzo, E., Foti, G., and Rimini, E. (1978), *Nucl. Instrum. Methods* **149**, 229.

Carlow, G.R., Barel, R.J., Zinke-Allmang, M. (1997), *Phys.Rev.B* **56(19),** 12519

Christensen, N.S., Jensen, F., Besenbacher, F., and Stensgaard, I. (1990), *Nucl. Instrum. Methods* **B51**, 97.

Cohen, C., Davies, J.A., Drigo, A.V., and Jackman, T.E. (1983), *Nucl. Instrum. Methods* **218**, 147.

Comedi, D., and Davies, J.A. (1992), *Nucl. Instrum. Methods* **B67**, 93.

Davies, J.A., and Norton, P.R. (1980), *Nucl. Instrum. Methods* **168**, 611.

Davies, J.A., Jackman, T.E., Eschbach, H.L., Domba, W., Wätjen, U., and Chivers, D. (1986), *Nucl. Instrum. Methods* **B15**, 238.

Doolittle, L.R. (1985), *Nucl. Instrum. Methods* **B9**, 344.

Doolittle, L.R. (1986), *Nucl. Instrum. Methods* **B15**, 227.

Edge, R.D. (1983), *IEEE Trans. Nucl. Sci.* **NS-30** (2), 1685.

El Bouanani, M., Pelicon, P., Razpet, A., Čadež, I., Budnar, M., Simčič, J., and Markelj, S. (2006), *Nucl. Instrum. Methods* **B243**, 392.

Eckstein, W., and Mayer, M. (1999), *Nucl. Instrum. Methods* **B153**, 337.

Ecker, K.H., Wätjen, U., Berger, A., Persson, L., Pritzkow, W., Radtke, M., and Riesemeier, H. (2002), *Nucl. Instrum. Methods* **B188**, 120.

Fischer, R., Mayer, M., von der Linden, W., and Dose, V. (1997), *Phys. Rev.* **E55**, 6667.

Gardner, R.P., and Wielopolski, L. (1977), *Nucl. Instrum. Methods* **140**, 289.

Geissel, H., Lennard, W.N., Ball, G.C., Forster, J.S., Lone, M.A., Milani, L., Phillips, D., and Plattner, H.H. (1984), *Nucl. Instrum. Methods* **230**, 770.

Giuntini, L., and Mando, P.A. (1994), *Nucl. Instrum. Methods* **B85**, 744.

Goulding, F.S., and Landis, D.A. (1982), *IEEE Trans. Nucl. Sci.* **NS-29**, 1125.

Grime, G.W., Sofield, C.J., Gomez-Morilla, I., Gwilliam, R., Ynsa, M.D., and Enguita, O. (2005), *Nucl. Instrum. Methods* **B231**, 378. This effect has also been observed in a poor vacuum.

Grubb, D.T. (1974), *J. Mater. Sci.* **9**, 1715.

GUM (1995), *Guide to the Expression of Uncertainty in Measurement*, BIPM/IEC/IFCC/ISO/IUPAC/IUPAP/OIML, identical to EN 13005:1999. See also the valuable Web site http://www.npl.co.uk/mathematics-scientific-computing/measurement-uncertainties/.

Gurbich, A.F., and Kornilov, N.V. (1991), *Nucl. Instrum. Methods* **B62**, 151.

Gurbich, A.F. (1995), *Nucl. Instrum. Methods* **A364**, 496.

Gurbich, A.F. (1996), *Nucl. Instrum. Methods* **B111**, 137.

Gurbich, A.F. (1997), *Nucl. Instrum. Methods* **B129**, 311.

Gurbich, A.F. (1998), *Nucl. Instrum. Methods* **B136–138**, 60.

Gurbich, A.F. (2000), *Nucl. Instrum. Methods* **B161–163**, 125.

Gurbich, A.F., and Molodtsov, S.L. (2004), *Nucl. Instrum. Methods* **B226**, 637.

Gurbich, A.F. (2004), *Nucl. Instrum. Methods* **B217**, 183.

Gurbich, A., and Jeynes, C. (2007), *Nucl. Instrum. Methods* **B265**, 447.

Gurbich, A. (2008), *Nucl. Instrum. Methods* **B266**, 1193.

Hemment, P.L.F., Singleton, J.F., and Stephens, K.G. (1975), *Thin Solid Films* **28**, L1.

Hautala, M., and Luomajarvi, M. (1980), *Radiat. Eff.* **45**, 159.

Huenges, E., Rösler, H., and Vonach, H. (1973), *Phys. Lett.* **B46** (3), 361.

IBANDL (2009), database at www-nds.iaea.org/ibandl maintained by A.F.Gurbich.

ICRU (1993), *Stopping Powers and Ranges for Protons and Alpha Particles*, ICRU Report 49, ICRU, Bethesda, MD.

Jeynes, C., and Kimber, A.C. (1985), *J. Phys. D.* **18**, L93.

Jeynes, C., Jafri, Z.H., Webb, R.P., Ashwin, M.J., and Kimber, A.C. (1997), *Surf. Interface Anal.* **25**, 254.

Jeynes, C., Barradas, N.P., Blewett, M.J., and Webb, R.P. (1998), *Nucl. Instrum. Methods* **B136–138**, 1229.

Jeynes, C., Barradas, N.P., Marriott, P.K., Boudreault, G., Jenkin, M., Wendler, E., and Webb, R.P. (2003), *J. Phys. D: Appl. Phys.* **36**, R97.

Jeynes, C., Peng, N., Barradas, N.P., and Gwilliam, R.M. (2006), *Nucl. Instrum. Methods* **B249**, 482.

Kim, J., Hong W, Woo HJ, Eum CH (2003), *J. Korean Phys. Soc.* **43**, 582.

Kirkpatrick, S., Gelatt Jr., C.D., and Vecchi, M.P. (1983), *Science* **220**, 671.

Konac, G., Kalbitzer, S., Klatt, C., Niemann, D., and Stoll, R. (1998), *Nucl. Instrum. Methods* **B136–138**, 159.

Knoll, G.F. (1989), *Radiation Detection and Measurement*, 2nd Ed., John Wiley and Sons, New York.

L'Ecuyer, J., Davies, J.A., and Matsunami, N. (1979), *Nucl. Instrum. Methods* **160**, 337.

Lee, W.P., Gundabala, V.R., Akpa, B.S., Johns, M.L., Jeynes, C., and Routh, A.F. (2006), *Langmuir* **22**, 5314.

Lennard, W.N., Geissel, H., Winterbon, K.B., Phillips, D., Alexander, T.K., and Forster, J.S. (1986), *Nucl. Instrum. Methods* **A248**, 454.

Lennard, W.N., Tong, S.Y., Mitchell, I.V., and Massoumi, G.R. (1989), *Nucl. Instrum. Methods* **B43**, 187.

Lennard, W.N., and Massoumi, G.R. (1990), *Nucl. Instrum. Methods* **B48**, 47.

Lennard, W.N., Massoumi, G.R., Simpson, T.W., and Mitchell, I.V. (1999), *Nucl. Instrum. Methods* **B152**, 370.

Marion, J.B. (1966), *Rev. Mod. Phys.* **38**, 660.

Mattauch, J.H.E., Thiele, W., and Wapstra, A.H. (1965), *Nucl. Phys.* **67**, 73.

Mayer, M., Fischer, R., Lindig, S., von Toussaint, U., Stark, R.W., and Dose, V. (2005), *Nucl. Instrum. Methods* **B228**, 349.

Mendenhall, M.H., and Weller, R.A. (1991), *Nucl. Instrum. Methods* **B58**, 11.

Möller, W., and Besenbacher, F. (1980), *Nucl. Instrum. Methods* **168**, 111.

Molodtsov, S.L., Gurbich, A.F., and Jeynes, C. (2008), *J. Phys. D: Appl. Phys.* **41**, 205303.

Morrison, R. (2007), *Grounding and Shielding: Circuits and Interference*, Wiley, New York.

Munnik, F., Plompen, A.J.M., Räisänen, J., and Wätjen, U. (1996), *Nucl. Instrum. Methods* **B119**, 445.

Niemann, D., Konac, G., and Kalbitzer, S. (1996), *Nucl. Instrum. Methods* **B118**, 11.

Pascual-Izarra, C., and Barradas, N.P. (2008), *Nucl. Instrum. Methods Phys. Res.* **B266**, 1866.

Pászti, F., Manuaba, A., Hajdu, C., Melo, A.A., and Da Silva, M.F. (1990), *Nucl. Instrum. Methods* **B47**, 187.

Paul, H., and Schinner, A. (2001), *Nucl. Instrum. Methods Phys. Res.* **B179**, 299.

Paul, H., and Schinner, A. (2002), *Nucl. Instrum. Methods Phys. Res.* **B195**, 166.

Paul, H., and Schinner, A. (2003), *Nucl. Instrum. Methods Phys. Res.* **B209** 252; see also Paul, H., and Schinner A. (2005), *Nucl. Instrum. Methods* **B227**, 461.

Paul, H., and Schinner, A. (2006), *Nucl. Instrum. Methods Phys. Res.* **B249**, 1.

Piel, N., Berheide, M., Polaczyk, C., Rolfs, C., and Schulte, W.H. (1994), *Nucl. Instrum. Methods* **A349** (1), 18.

Pritzkow, W., Vogl, J., Berger, A., Ecker, K., Grötzschel, R., Klingbeil, P., Persson, L., Riebe, G., and Wätjen, U. (2001), *Fresenius J. Anal. Chem.* **371**, 867.

Polanyi, M. (1958), *Personal Knowledge*, Chicago University Press, Chicago, IL. I quote from the 1974 paperback edition, chap. 2, p. 19. A beautiful book, invaluable for those who want to know how we know what we know.

Radeka, V. (1988), *Annu. Rev. Nucl. Part. Sci.* **38**, 217.

Reinholz, U., Bremser, W., Brzezinka, K.W., Strub, E., Weise, H.P., and Merchel, S. (2008), *Nucl. Instrum. Methods* **B266**, 2418.

Roush, M.L., West, M.A., and Marion, J.B. (1970), *Nucl. Phys.* **A147**, 235.

Schultz, P.J., Jagadish, C., Ridgway, M.C., Elliman, R.G., and Williams, J.S. (1991), *Phys. Rev.* **B44**, 9118.

Seah, M.P., David, D., Davies, J.A., Jeynes, C., Ortega, C., Read, P.M., Sofield, C.J., and Weber, G. (1988), *Nucl. Instrum. Methods* **B30**, 140.

SigmaCalc (2009), database and program at www-nds.iaea.org/sigmacalc built by A.F. Gurbich.

Sitter, C., Davies, J.A., Jackman, T.E., and Norton P.R. (1982), *Rev. Sci. Instrum.* **53**, 797.

Sjöland, K.A., Munnik, F., Chaves, C., and Wätjen, U. (1999), *Nucl. Instrum. Methods* **B150**, 69.

Sjöland, K.A., Munnik, F., and Wätjen, U. (2000), *Nucl. Instrum. Methods* **B161**, 275.

Smyth, D.M. (1966), *J. Electrochem. Soc.* **113**, 1271.

Szilágyi, E., Pászti, F., and Amsel, G. (1995), *Nucl. Instrum. Methods* **B100**, 103.

Tesmer, J.R., and Nastasi, M. (eds.) (1995), *Handbook of Modern Ion Beam Materials Analysis*, Materials Research Society, Pittsburgh, PA.

Tombrello, T.A. (1984), *Nucl. Instrum. Methods* **B2**, 555.

van Lieshout, R., Wapstra, A.H., Ricci, R.A., and Girgis, R.K. (1966), "Scintillation spectra analysis", in *Alpha-, beta- and gamma-ray spectroscopy* (Siegbahn, K., ed.), North-Holland, Amsterdam, p. 515.

Venkatesan, T., Brown, W.L., and Wilkens, B.J. (1984), *Nucl. Instrum. Methods* **Bl**, 605.

Wang, Y.Q., Liso, C.G., Yang, S.S., and Zheng, Z.H. (1990), *Nucl. Instrum. Methods* **B47**, 427.

Wätjen, U., and Bax, H. (1994), *Nucl. Instrum. Methods* **B85**, 627.

Weber, W.J., Ewing, R.C., Angell, C.A., Arnold, G.W., Cormack, A.N., Delaye, J.M., Griscom, D.L., Hobbs, L.W., Navrotsky, A., Price, D.L., Stoneham, A.M., and Weinberg, W.C. (1997), *J. Mater. Res.* **12** (8), 1946.

Wielopolski, L., and Gardner, R.P. (1976), *Nucl. Instrum. Methods* **133** 303.

Wielopolski, L., and Gardner, R.P. (1977), *Nucl. Instrum. Methods* **140**, 297.

Williams, J.S., and Möller, W. (1978), *Nucl. Instrum. Methods* **157** (2),: 213.

White, R.E., Barker, P.H., and Lovelock, D.M.J. (1985), *Metrologia* **21**, 193.

Ziegler, J.F. (2004), *Nucl. Instrum. Methods* **B219–220**, 1027; also see www.srim.org.